END
DATE
FILMED
4 -78
DDC

1.0

1.1

1.25   1.4   1.6

4.5
5.0
5.6
3.2
3.6
4.0

2.8   2.5

3.2   2.2

2.0

1.8

MICROCOPY RESOLUTION TEST CHART
NATIONAL BUREAU OF STANDARDS-1963-A

AD-E300105

DNA 3961F-6

AD A051290

CHARACTERIZATION OF THE DYNAMIC BEHAVIOR OF POROUS SOLIDS

Part 6–Dynamic Response of Porous Ceramics – Experiments

⑫

SRI International

333 Ravenswood Avenue

Menlo Park, California 94025

March 1976

Final Report for Period 14 January 1974–31 January 1976

CONTRACT No. DNA 001-74-C-0150

Prepared for
Director
DEFENSE NUCLEAR AGENCY
Washington, D. C. 20305

DDC

RECEIVED
MAR 17 1978
B

Destroy this report when it is no longer
needed. Do not return to sender.

UNCLASSIFIED

REPORT DOCUMENTATION PAGE		READ INSTRUCTIONS BEFORE COMPLETING FORM
1. REPORT NUMBER DNA 3961F-6	2. GOVT ACCESSION NO.	3. RECIPIENT'S CATALOG NUMBER
4. TITLE (and Subtitle) CHARACTERIZATION OF THE DYNAMIC BEHAVIOR OF POROUS SOLIDS. Part 6. Dynamic Response of Porous Ceramics—Experiments.		5. TYPE OF REPORT & PERIOD COVERED Final Report, 14 Jan 74—31 Jan 76
		6. PERFORMING ORG. REPORT NUMBER PYU-3163
7. AUTHOR(s) D. C. Erlich Author D. R. Curran Supervisor		8. CONTRACT OR GRANT NUMBER(s) DNA 001-74-C-0150
9. PERFORMING ORGANIZATION NAME AND ADDRESS SRI International 333 Ravenswood Avenue Menlo Park, California 94025		10. PROGRAM ELEMENT, PROJECT, TASK AREA & WORK UNIT NUMBERS Subtask N99QAXAC308-40
11. CONTROLLING OFFICE NAME AND ADDRESS Director Defense Nuclear Agency Washington, D.C. 20305		12. REPORT DATE Mar 76
		13. NUMBER OF PAGES 58
14. MONITORING AGENCY NAME & ADDRESS(if different from Controlling Office)		15. SECURITY CLASS (of this report) UNCLASSIFIED
		15a. DECLASSIFICATION/DOWNGRADING SCHEDULE

16. DISTRIBUTION STATEMENT (of this Report)

Approved for public release; distribution unlimited.

17. DISTRIBUTION STATEMENT (of the abstract entered in Block 20, if different from Report)

19. KEY WORDS (Continue on reverse side if necessary and identify by block number)

Porous Ceramic   Lagrangian Gage Technique
Alumina   Constitutive Paths
Hafnium Titanate

20. ABSTRACT (Continue on reverse side if necessary and identify by block number)

High pressure dynamic stress wave experiments were performed on sintered alumina of several initial porosities and the multiple Lagrangian gage technique was used to record stress and particle velocity histories at several locations within the specimen in order to calculate the constitutive loading and unloading paths. We now have a family of such paths (shown in Figure 10) that can be used to construct an equation-of-state surface for a predictive hydrodynamic computer code.

DD FORM 1473   EDITION OF 1 NOV 65 IS OBSOLETE
1 JAN 73

UNCLASSIFIED

20. ABSTRACT (Continued)

The results show that sintered alumina with initial porosities ranging from 20% to 45% exhibit no significant time-dependence in their constitutive relations when shocked to peak pressure of hundreds of kbar (where the precursor is overdriven). When shocked to pressures slightly above the Hugoniot elastic limit, however, a time-dependent response does exist (see Figures A-9 and A-10). Further experiments would be needed to give us an accurate predictive capability in this region.

We performed a few experiments on flame-sprayed alumina and flame-sprayed hafnium titanate, which yield constitutive paths in the region below 7 kbar.

```
ACCESSION for
NTIS         White Section
DDC          Buff Section
UNANNOUNCED
JUSTIFICATION

BY
DISTRIBUTION/AVAILABILITY CODES
Dist.    AVAIL. and/or SPECIAL

A
```

PREFACE

This report is Volume 6 in a seven-volume series on Characterization of the Dynamic Behavior of Porous Solids. The titles and authors of the individual reports in the series are:

	Title	Authors
Volume 1	Summary of Results	D. R. Curran, R. E. Tokheim, M. J. Ginsberg, L. Seaman, A. B. Lutze, D. C. Erlich, J. T. Rosenberg, and D. A. Shockey
Volume 2	Computational Models for Predicting the Dynamic Stress Response of Some Porous Ceramics in a Radiation Environment	R. E. Tokheim
Volume 3	Computational Model for Predicting the Dynamic Stress Response of Porous Beryllium in a Radiation Environment	R. E. Tokheim
Volume 4	Electron Beam Studies of Porous Beryllium and Porous Ceramics	A. B. Lutze
Volume 5	Dynamic Response of Porous Beryllium-Experiments	J. T. Rosenberg
Volume 6	Dynamic Response of Porous Ceramics-Experiments	D. C. Erlich
Volume 7	Microstructural Characterization of Several Porous Ceramics and Porous Beryllium	D. A. Shockey and J. P. Wilhelm

1

Conversion factors for U.S. customary to metric (SI) units of measurement.

To Convert From	To	Multiply By
angstrom	meters (m)	$1.000\ 000 \times E\ -10$
atmosphere (normal)	kilo pascal (kPa)	$1.013\ 25 \times E\ +2$
bar	kilo pascal (kPa)	$1.000\ 000 \times E\ +2$
barn	meter^2 (m^2)	$1.000\ 000 \times E\ -28$
British thermal unit (thermochemical)	joule (J)	$1.054\ 350 \times E\ +3$
calorie (thermochemical)	joule (J)	$4.184\ 000$
cal (thermochemical)/cm^2	mega joule/m^2 (MJ/m^2)	$4.184\ 000 \times E\ -2$
curie	*giga becquerel (GBq)	$3.700\ 000 \times E\ +1$
degree (angle)	radian (rad)	$1.745\ 329 \times E\ -2$
degree Fahrenheit	degree kelvin (K)	$t_K = (t^\circ f + 459.67)/1.8$
electron volt	joule (J)	$1.602\ 19 \times E\ -19$
erg	joule (J)	$1.000\ 000 \times E\ -7$
erg/second	watt (W)	$1.000\ 000 \times E\ -7$
foot	meter (m)	$3.048\ 000 \times E\ -1$
foot-pound-force	joule (J)	$1.355\ 818$
gallon (U.S. liquid)	meter^3 (m^3)	$3.785\ 412 \times E\ -3$
inch	meter (m)	$2.540\ 000 \times E\ -2$
jerk	joule (J)	$1.000\ 000 \times E\ +9$
joule/kilogram (J/kg) (radiation dose absorbed)	Gray (Gy)	$1.000\ 000$
kilotons	terajoules	4.183
kip (1000 lbf)	newton (N)	$4.448\ 222 \times E\ +3$
kip/inch^2 (ksi)	kilo pascal (kPa)	$6.894\ 757 \times E\ +3$
ktap	newton-second/m^2 (N-s/m^2)	$1.000\ 000 \times E\ +2$
micron	meter (m)	$1\ 000\ 000 \times E\ -6$
mil	meter (m)	$2.540\ 000 \times E\ -5$
mile (international)	meter (m)	$1.609\ 344 \times E\ +3$
ounce	kilogram (kg)	$2.834\ 952 \times E\ -2$
pound-force (lbs avoirdupois)	newton (N)	$4.448\ 222$
pound-force inch	newton-meter (N·m)	$1.129\ 848 \times E\ -1$
pound-force/inch	newton/meter (N/m)	$1.751\ 268 \times E\ +2$
pound-force/foot^2	kilo pascal (kPa)	$4.788\ 026 \times E\ -2$
pound-force/inch^2 (psi)	kilo pascal (kPa)	$6.894\ 757$
pound-mass (lbm avoirdupois)	kilogram (kg)	$4.535\ 924 \times E\ -1$
pound-mass-foot^2 (moment of inertia)	kilogram-meter^2 (kg·m^2)	$4.214\ 011 \times E\ -2$
pound-mass/foot^3	kilogram/meter^3 (kg/m^3)	$1.601\ 846 \times E\ +1$
rad (radiation dose absorbed)	**Gray (Gy)	$1.000\ 000 \times E\ -2$
roentgen	coulomb/kilogram (C/kg)	$2.579\ 760 \times E\ -4$
shake	second (s)	$1.000\ 000 \times E\ -8$
slug	kilogram (kg)	$1.459\ 390 \times E\ +1$
torr (mm Hg, 0° C)	kilo pascal (kPa)	$1.333\ 22 \times E\ -1$

*The becquerel (Bq) is the SI unit of radioactivity; 1 Bq = 1 event/s.
**The Gray (Gy) is the SI unit of absorbed radiation.

A more complete listing of conversions may be found in "Metric Practice Guide E 380-74," American Society for Testing and Materials.

CONTENTS

ILLUSTRATIONS

4

TABLES

I IMPACT EXPERIMENTS

The main objective of this phase of the program was to perform a set of dynamic loading experiments on sintered alumina* to generate equation-of-state paths that would be used to construct the stress-volume-energy equation-of-state surface. The stress and energy regions selected for study were those attainable with available techniques, namely, gas gun and high explosives (HE) loading, and those expected to yield the most valuable information for determination of parameters, such as yield strength, and the shape of the equation-of-state surface. The secondary objective was to perform a few experiments on several other porous ceramics, including flame-sprayed alumina* and flame-sprayed hafnium titanate* to obtain a first estimate of some of their equation-of-state characteristics.

We performed eleven dynamic loading experiments on sintered alumina and six on the flame-sprayed alumina and hafnium titanate. Our experimental method was the multiple embedded Lagrangian gage technique, which, together with the Lagrangian gage analysis, forms the most powerful technique currently available for determining the equation-of-state paths followed by any relatively homogeneous material (that is, a material in which the largest inhomogeneities are small with respect to the thickness in the direction of stress wave propagation) subject to high-pressure transient loading. The Lagrangian technique has been used successfully at SRI in the study of complex materials, such as rocks and soils,[1-4] liquids,[5] metals,[6] and composites.[7] The technique is based

---

*These materials are more fully described in Part 7 of this series.

on the simultaneous measurement of stress or particle velocity histories at several Lagrangian locations within the material of interest. These histories form a surface in stress-Lagrangian position-time or particle velocity-Lagrangian position-time 3-space, along which the differential equations of mass, momentum, and energy conservation can be integrated to calculate the specific volume, internal energy, or any other desired equation-of-state parameter at any point on this surface.[8,9] Thus, the equation-of-state path that the material follows at any position within the region of stress or particle velocity measurement can be determined throughout the complete loading and unloading cycle in one experiment. This technique therefore substantially increases the amount of data obtained per shot over the standard Hugoniot experiments, which yield only a Hugoniot stress point, a shock velocity, and perhaps an initial unloading velocity.

Although the Lagrangian analysis was originally developed for use with materials exhibiting simple, time-independent flow, it has recently been extended to the point where no limitations at all are placed on the type of flow involved (except that the material undergoes one-dimensional strain in the region of measurement).[10] Therefore, materials can now be studied that exhibit any complex or time-dependent constitutive behavior, and furthermore this study can be carried out in a region undergoing stress attenuation.

II EXPERIMENTAL PROCEDURES

To obtain simultaneous measurement of stress or particle velocity histories at several depths within a material undergoing transient loading, one needs to slice the material of interest into slabs perpendicular to the direction of stress wave propagation, and position stress or particle velocity gages in between each slab, making the gage package as thin as possible to reduce the perturbation of the flow by the gage. The loading may result either from the planar impact of a projectile launched by a gas gun, by high explosives, or by detonation of high explosives placed in contact with the material.

The two SRI gas guns are capable of reaching peak stresses of approximately 100 kbar in porous ceramics. In-contact explosives are capable of pressures up to $\sim$ 400 kbar. Three different high explosives were used in this program: PBX 9404 and Comp B, to obtain peak stresses in the range from 250-400 kbar; and Baratol, to reach from 60-120 kbar.

Although several simultaneous stress histories or particle velocities alone would be sufficient to determine the equation-of-state paths, we decided to use both stress gages and particle velocity gages whenever possible to increase the probability of obtaining good data and to provide a means of cross-checking results.

Electromagnetic foil particle velocity gages were used to record particle velocity histories. They are based on the principle that a conductor moving at a right angle to a uniform magnetic field generates a voltage (V) across its length (ℓ) that is directly proportional to its velocity (u), the constants of proportionality being simply the product of the magnetic field strength (B) and its length in the direction

9

mutually perpendicular to its velocity and the magnetic field, i.e.,
$V = u \ell B$.

Manganin gages were used to record stress histories in the region above 40 kbar and ytterbium foil gages in the region below 40 kbar. These gages are piezoresistant transducers, whose resistance changes as a function of the applied stress in a more-or-less known way. Ytterbium has been calibrated extensively in both loading and unloading in the range from 0 to 33.4 kbar,[11] while the piezoresistance coefficient of manganin is known to less accuracy, particularly at higher pressures and during unloading. The disadvantages of using stress gages as opposed to particle velocity gages are (1) the stress gage calibration is based on complex material properties of the gage itself which need to be determined, while the particle velocity gage output is based entirely on geometry; and (2) the stress gage is sensitive to changes in resistivity of the adjacent materials caused by high pressures and temperatures present in HE experiments, whereas the particle velocity gage is not. The main advantage of the stress gages is that the analysis seems to be less sensitive to the numerical approximation or the fitting procedures used.[10]

Table 1 lists all the dynamic loading experiments performed in this phase of the program, along with some of the basic experimental parameters. In the first eleven shots, sintered alumina was used. Three differential initial porosities of this material were selected, nominally 20%, 30%, and 45%, to attain different internal energies on loading, as shown in Figure 1. The higher the initial porosity, the higher the internal energy achieved during compression to the same stress. Of the last six shots, five used flame-sprayed alumina, and one used flame-sprayed hafnium titanate.
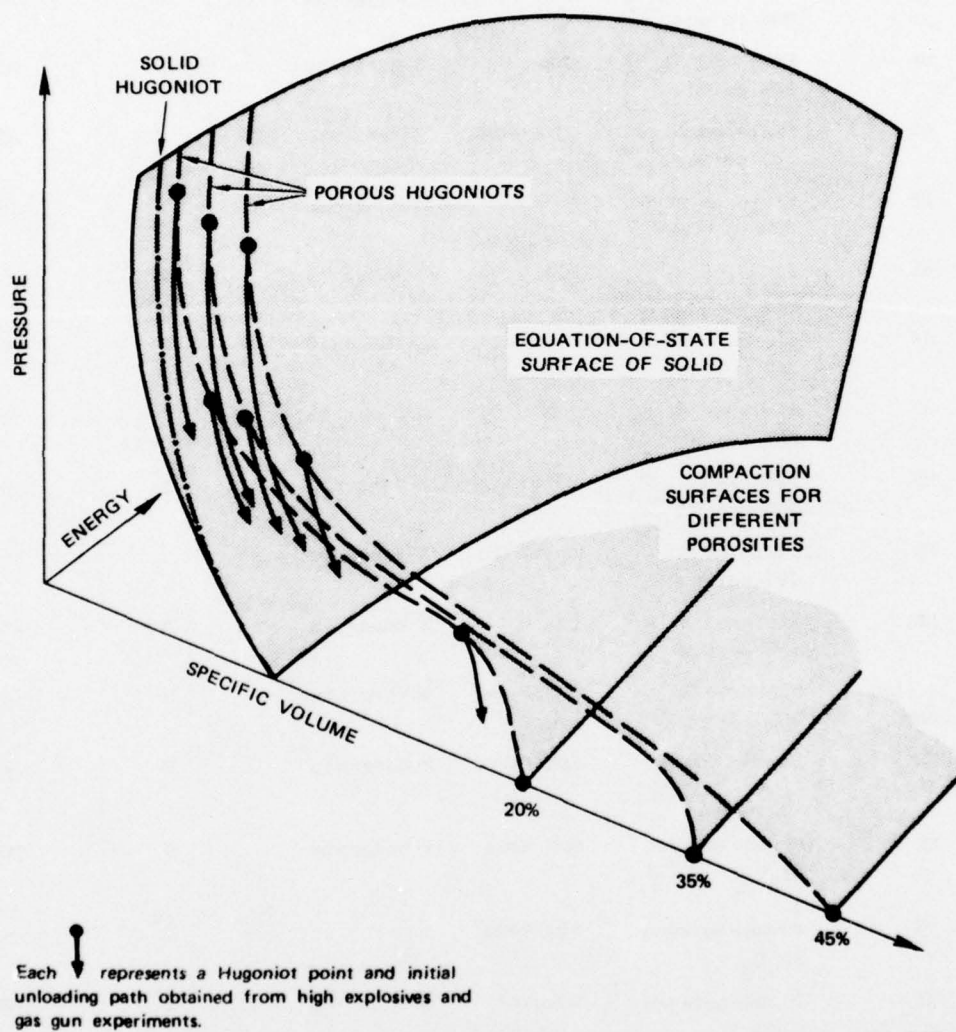
Figure 2 shows a schematic diagram for all the HE experiments on the baseline material. The target consists of four sintered alumina

Table 1

DYNAMIC LOADING EXPERIMENTS AND EXPERIMENTAL PARAMETERS

Shot No.	Type of Loading	Material Used	HE Used or Proj. Vel.	No. of Stress Gage Planes & Gage Mat'l	No. of Particle Vel. Gage Planes	Approx. Peak Stress (kbar)
1	HE	Sintered Al_2O_3 20% porous	PBX 9404	3 Manganin	3	370
2	HE	Sintered Al_2O_3 20% porous	Comp B	3 Manganin	3	350
3	HE	Sintered Al_2O_3 20% porous	PBX 9404	3 Manganin	3	360
4	HE	Sintered Al_2O_3 20% porous	Baratol	3 Manganin	3	120
5	HE	Sintered Al_2O_3 35% porous	PBX 9404	3 Manganin	3	310
6	HE	Sintered Al_2O_3 35% porous	Baratol	3 Manganin[*]	3	90
8	HE	Sintered Al_2O_3 45% porous	PBX 9404	3 Manganin[*]	3[*]	65
9	HE	Sintered Al_2O_3 35% porous	Baratol	3 Manganin	3[*]	90
10	HE	Sintered Al_2O_3 45% porous	Baratol	3 Manganin	3	65
11	HE	Sintered Al_2O_3 45% porous	PBX 9404	3 Manganin[*]	3	270
51	4" Gas Gun	Sintered Al_2O_3 20% porous	0.360 mm/ μsec	3 Ytterbium[*]	3	40
101	HE	Flame-sprayed Al_2O_3	PBX 9404	2 Manganin[*]	0	-
102	HE	Flame-sprayed Al_2O_3	PBX 9404	2 Manganin[*]	0	325
103	HE	Flame-sprayed Al_2O_3	PBX 9404	0	2[*]	-
104	HE	Flame-sprayed Al_2O_3	Baratol	0	2[*]	100
151	2½" Gas gun	Flame-sprayed Al_2O_3	0.163 mm/ μsec	3 Ytterbium	0	5
152	2½" Gas gun	Flame-sprayed Hafnium titanate	0.092 mm/ μsec	3 Ytterbium	0	7

[*] Indicates gage records are for one of a variety of reasons not amenable to a Lagrangian analysis (see Appendix).

11

Each ▼ represents a Hugoniot point and initial
unloading path obtained from high explosives and
gas gun experiments.

MA-2407-9

FIGURE 1   SCHEMATIC DEPICTION OF CONSTITUTIVE PATHS OBTAINED
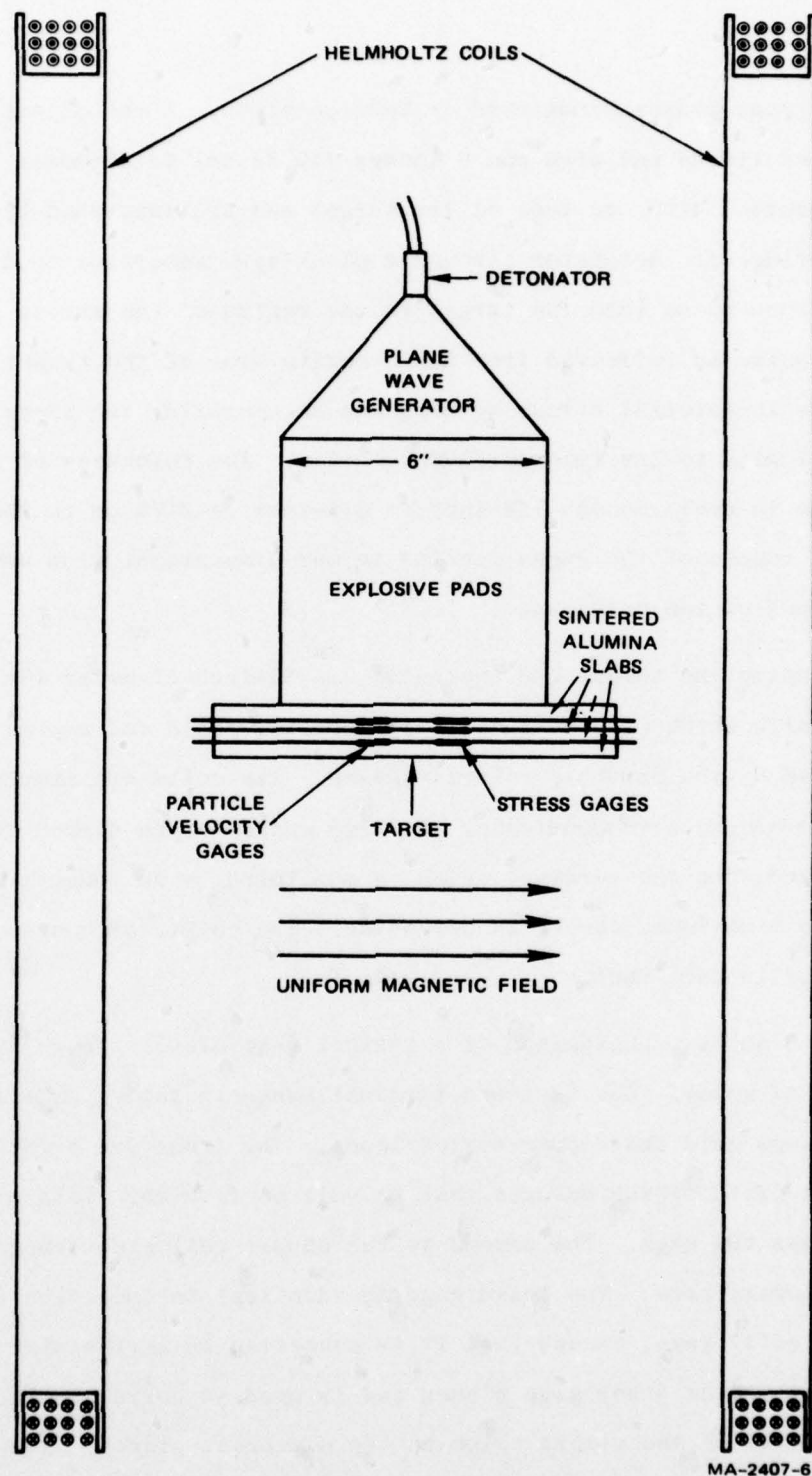BY LOADING DIFFERENT INITIAL POROSITIES

HELMHOLTZ COILS

DETONATOR

PLANE
WAVE
GENERATOR

6"

EXPLOSIVE PADS

SINTERED
ALUMINA
SLABS

PARTICLE
VELOCITY
GAGES

TARGET

STRESS GAGES

UNIFORM MAGNETIC FIELD

MA-2407-6

FIGURE 2   SCHEMATIC DIAGRAM OF H.E. EXPERIMENTS WITH SINTERED ALUMINA

13

slabs, with gage planes sandwiched in between slabs. A set of explosive pads 6 inches (15.24 cm) high and 6 inches (15.24 cm) in diameter are placed in contact with one face of the target and are initiated by an exploding-bridgewire detonator through a plane-wave generator to induce a planar stress pulse into the target in the region of the stress gages. The stress pulse is reflected from the opposite side of the target reducing the in-material stress to zero and accelerating the in-material particle velocity to the free surface velocity. The thickness of the target slabs is small enough (1/8-inch to 3/8-inch or .3175 cm to .9525 cm) so that the region of the gages remains in one-dimensional flow until nearly the end of the unloading.

Surrounding the target and explosive are 32-inch-diameter (81.28 cm) Helmholtz coils which create the uniform magnetic field (of approximately 500 G) needed by the particle velocity gages. The coils are simply copper wire wrapped around a wooden frame. A large capacitor is dumped through the coils, and when the current, which is monitored by an inductive probe, builds up to a maximum, the HE is detonated. The coils, of course, are destroyed in each shot.

Figure 3 shows a photograph of a typical gage plane. There are three types of gages. One is the 4-terminal manganin foil gage with a 1/4-inch square grid and copper-coated leads. The leads are parallel to the magnetic field, which ensures that no voltage from the field will be induced across the gage. The second is the copper foil electromagnetic particle velocity gage. The third gage is identical in operation to the particle velocity gage, except that it is connected in series with similar gages in the other gage planes and is used to correlate the times of arrival of the stress pulse at the different planes. All the gages were recorded on oscillographs using a differential mode, and the standard constant current pulsed-power supply recording system[12] was used for the stress gages.

14

MP-2407-5

MANGANIN STRESS
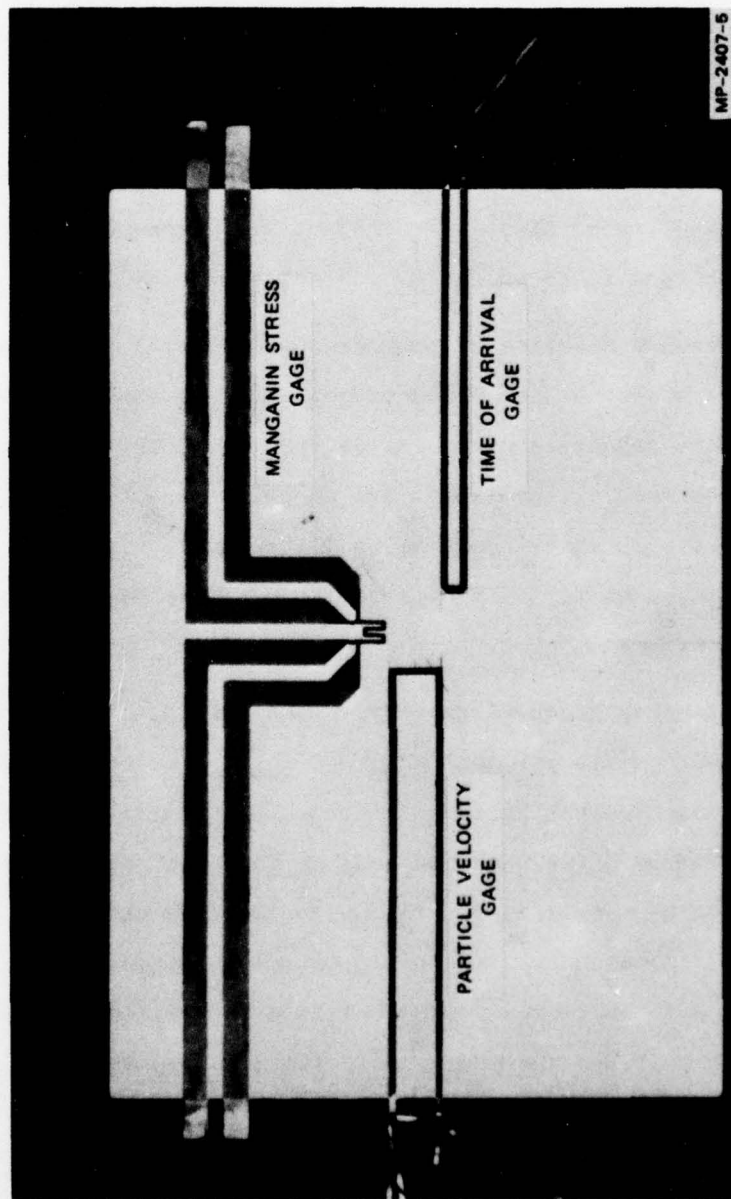GAGE

TIME OF ARRIVAL
GAGE

PARTICLE VELOCITY
GAGE

FIGURE 3   TYPICAL GAGE PLAN IN H.E. ALUMINA EXPERIMENTS

For most of the shots, no insulating material was used. The gages were simply glued to one of the slabs, and the adjacent slab was pressed on with a thin layer of vacuum grease to eliminate air pockets. The surfaces of the alumina slabs were first coated with a sealer so that nothing would seep into the pores. The total gage package thickness was approximately 0.004 inch (.01 cm). On two of the Shots (2 and 11), the gages were encapsulated between thin sheets of mica in an attempt to reduce the shunting of the stress gages by the decrease in resistivity of the various gage package materials. In these shots the gage package thickness varied from 0.006 inch (.015 cm) to 0.014 inch (.0356 cm).

Figure 4 presents a series of photographs depicting the experimental setup. Figure 4a shows the assembled target with all the cables attached, Figure 4b shows the target in place inside the Helmholtz coils (the two dark points on the face of the target are co-axial pins flush with the surface, which are used to trigger the oscilloscopes), Figure 4c shows the explosives positioned on top of the target, and Figure 4d, the complete assembly before firing.

The HE experiments on the flame-sprayed materials were similar to those on the baseline material, but scaled down in size because of the smaller size of target slabs available (from 3.81 to 4.45 cm squares and from 0.127 to 0.203 cm thick) and the need to maintain one-dimensional flow in the region of measurement. The explosive pads used were reduced to 2 inches (5.08 cm) high by 2 inches (5.08 cm) in diameter, the Helmholtz coils were reduced to 16 inches (40.64 cm) in diameter, only three slabs were used in each shot, so there were only two gage planes, and only one gage, a manganin stress gage or a particle velocity gage, could fit in each gage plane.

Figure 5 depicts a schematic diagram for the gas gun experiment on the baseline material (Shot 51). SRI's 4-inch (10.16 cm)-diameter helium
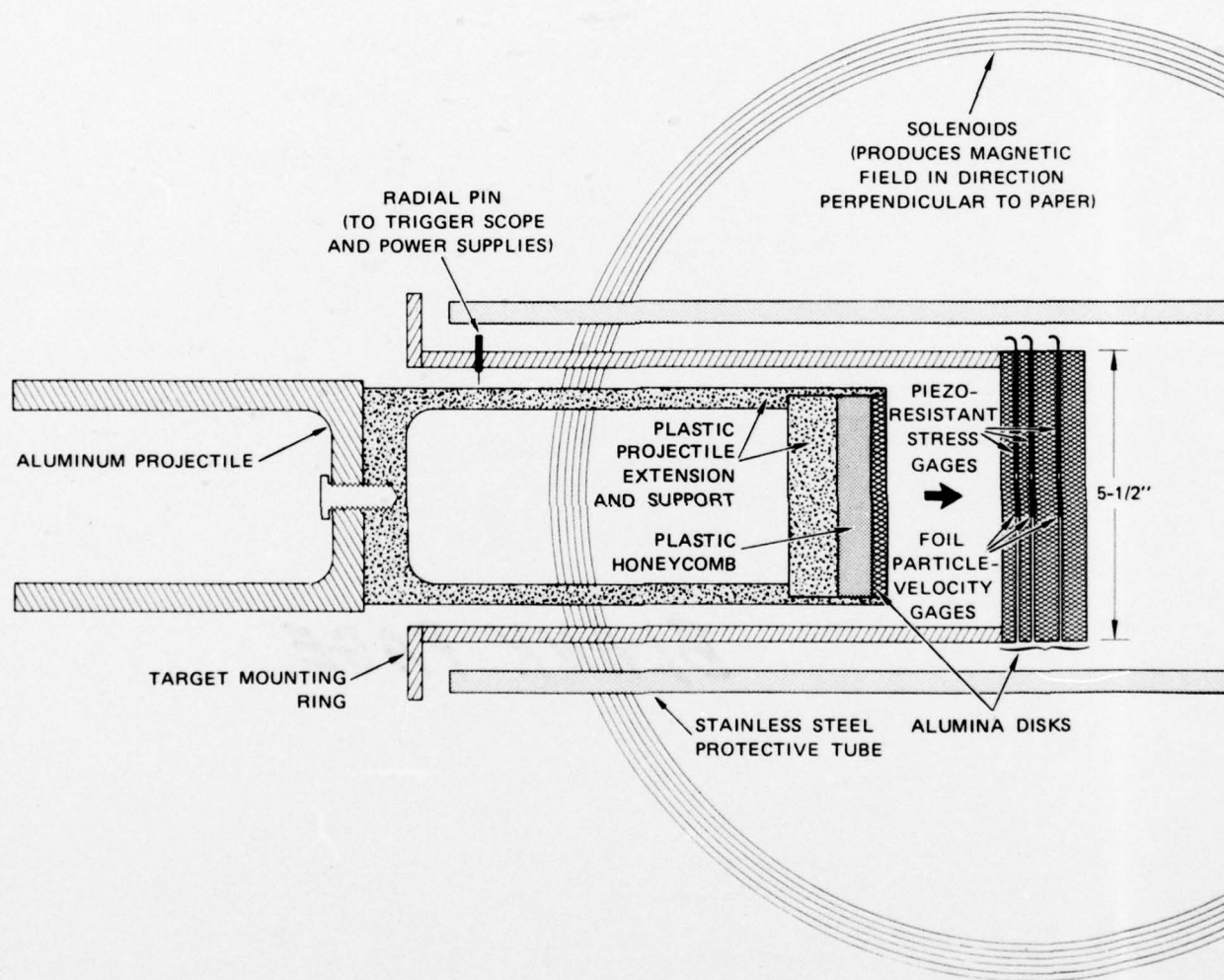
16

(b)

(d)

(a)

(c)
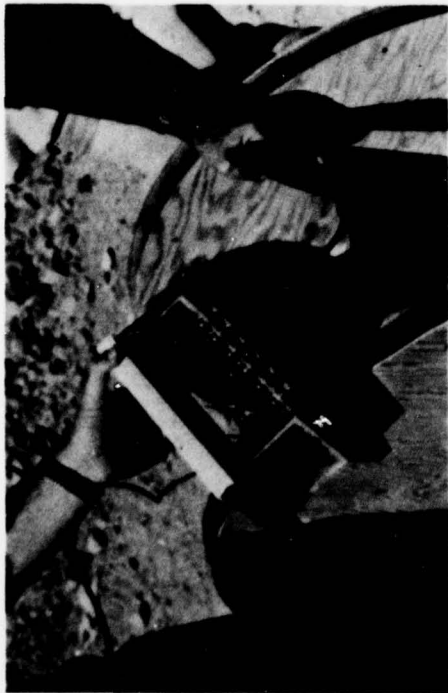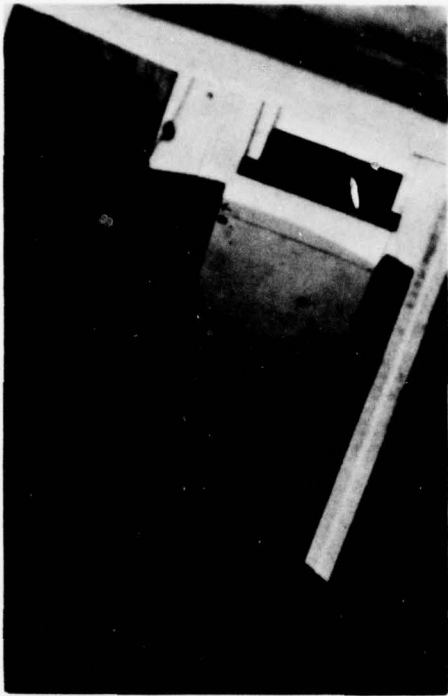
MP-2407-31

FIGURE 4 FINAL PREPARATION OF H.E. ALUMINA EXPERIMENTS

17

gas gun was used to launch a projectile with a thin head of sintered alumina into a target consisting of four 5-1/2-inch (13.97 cm)-diameter sintered alumina disks with three stress and particle velocity gage planes sandwiched in between the disks. On impact, compressional waves were sent into the target and into the projectile head; reflection of the latter wave at the rear surface of the projectile head produced a rarefaction which unloaded the target to zero stress (the plastic honeycomb projectile head backing has a negligibly small shock impedance compared with that of the alumina).

The stress and particle velocity gages are identical in operation to those used in the HE experiments. Ytterbium was used here in place of manganin as the piezoresistive element to obtain higher sensitivity. The uniform magnetic field was produced by an electromagnetic solenoid system, described in detail in Reference 4. A nonmagnetic stainless steel tube surrounded the target to protect the magnet from flying fragments.

The two gas gun shots on the flame-sprayed material (Shots 151 and 152) were similar except that the 2-1/2-inch (6.35 cm)-diameter gas gun and only stress gages were used.
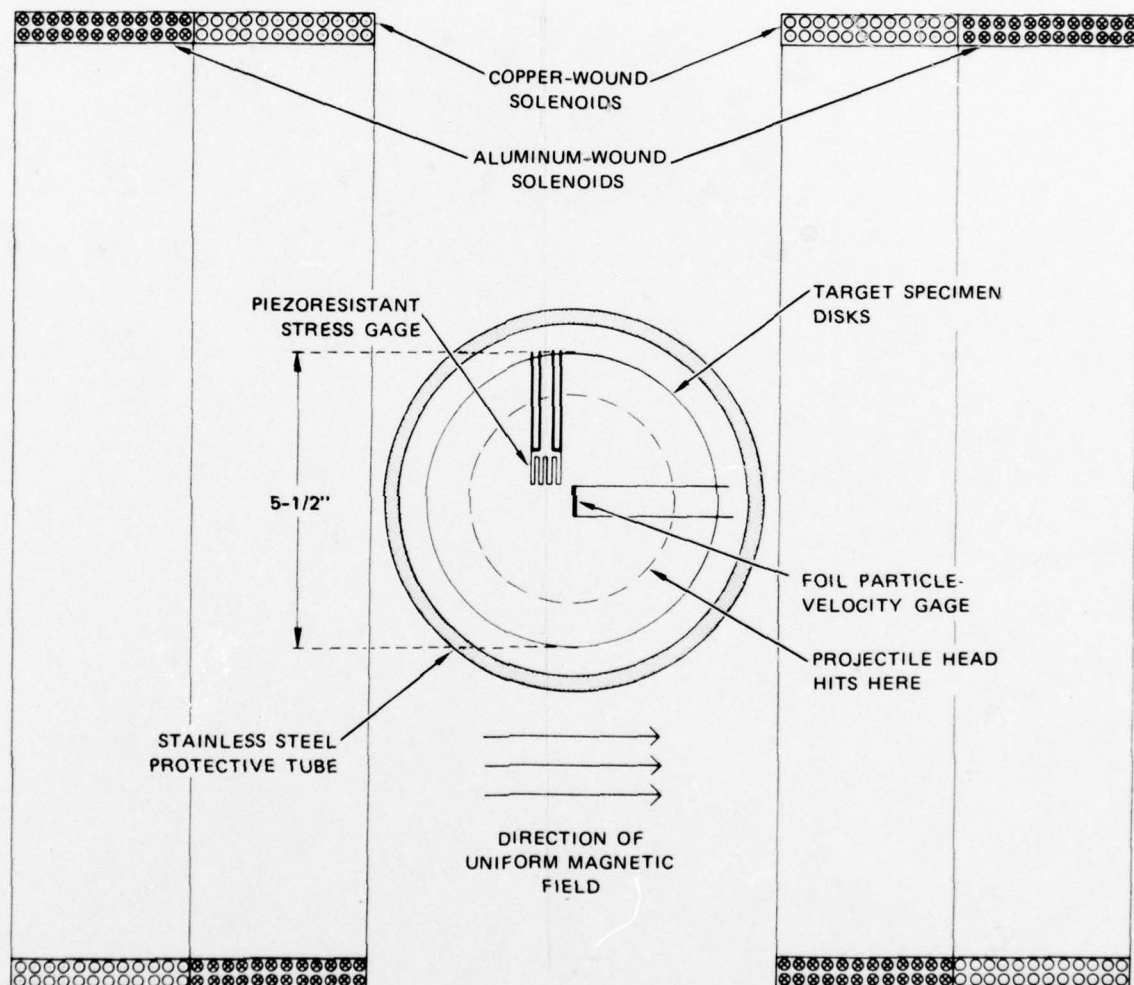
(a) SIDE VIEW

COPPER-WOUND
SOLENOIDS

ALUMINUM-WOUND
SOLENOIDS

PIEZORESISTANT
STRESS GAGE

TARGET SPECIMEN
DISKS

5-1/2"

FOIL PARTICLE-
VELOCITY GAGE

PROJECTILE HEAD
HITS HERE

STAINLESS STEEL
PROTECTIVE TUBE

DIRECTION OF
UNIFORM MAGNETIC
FIELD
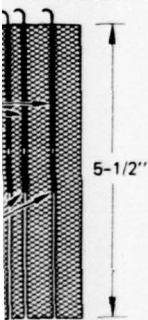
(b) FRONT VIEW

MP-1139-11C

FIGURE 5   EXPERIMENTAL SETUP
FOR GAS GUN SHOTS

19

III EXPERIMENTAL RESULTS AND ANALYSIS

Of the eleven dynamic experiments performed on sintered alumina, nine yielded particle velocity gage records and seven yielded stress gage records that were satisfactory for Lagrangian analysis. Of the six shots using the flame-sprayed alumina and flame-sprayed hafnium titanate, only the two gas-gun shots yielded analyzable stress gage records. For all the shots analyzed, Table 2 lists the measured ceramic densities and the distances from the impact plane or HE interface for each of the gage planes.

As an example of the raw data, Figure 6 shows oscillographs from the three particle velocity gages and three stress gages in Shot 1. In this shot, 20% porous alumina was shocked to a peak stress of approximately 370 kbar, and the gage results are typical of all the shots in this high-stress region. The blank spots on the gage records are 1 μsec apart.

The particle velocity gages exhibit a small precursor, a rapid rise to the peak particle velocity, a very slight decay owing to the Taylor wave (the gradual relief wave following the detonation of an explosive) and an acceleration to the free surface velocity when the relief wave from the back of the target arrives. For a porous material, the free surface velocity can be much less than twice the peak particle velocity.

The stress gages exhibit a practically negligible precursor, a rapid rise to the peak stress, a gradual but significant decay owing to the Taylor wave, and then a more rapid relief to zero stress. The stress gage records do not return to their original level after release to zero stress because of hysteresis--the permanent change in the gage resistance

21

Table 2

CONFIGURATIONS AND DIMENSIONS FOR
DYNAMIC LOADING EXPERIMENTS

HE SHOTS
GAS GUN SHOTS
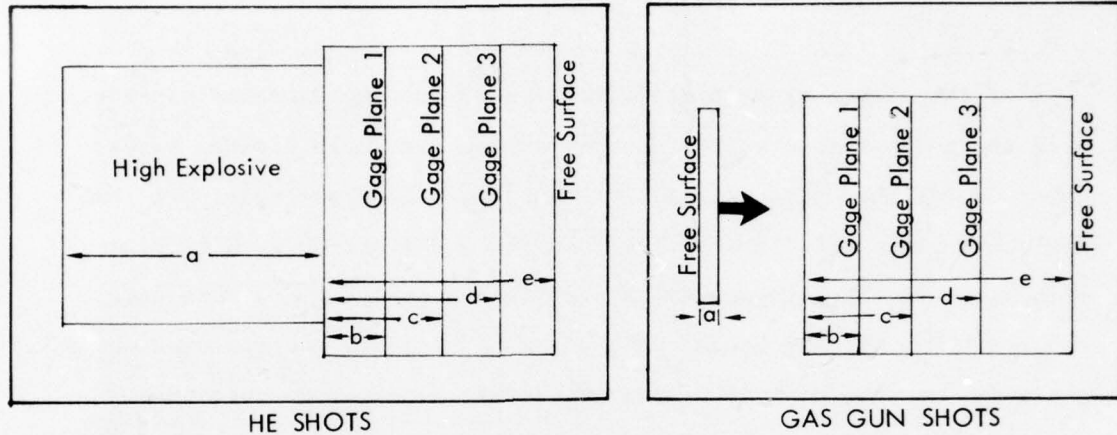
Shot No.	Type	Ceramic Density (gm/cm^3)	Shot Dimensions (cm)				
			a	b	c	d	e
1	HE	3.16	15.24	0.712	1.109	1.502	1.895
2	HE	3.17	15.24	0.715	1.123	1.531	1.923
3	HE	3.15	15.24	0.706	1.095	1.479	1.854
4	HE	3.16	15.24	0.706	1.086	1.476	2.169
5	HE	2.61	15.24	0.953	1.336	1.718	2.107
6	HE	2.59	15.24	0.950	1.330	1.714	2.103
9	HE	2.61	15.24	0.952	1.339	1.776	2.437
10	HE	2.21	15.24	0.949	1.355	1.762	2.482
11	HE	2.22	15.24	0.953	1.364	1.774	2.177
51	Gas gun	3.16	0.366	0.380	0.763	1.151	1.854
151	Gas gun	2.78	0.063	0.156	0.326	0.483	0.773
152	Gas gun	6.97	0.072	0.171	0.363	0.555	0.888

22

STRESS GAGES

Mn1

Mn2

Mn3

MP-2407-1

HIGH
EXPLOSIVES:
PBX 9404

20% POROUS ALUMINA

PARTICLE VELOCITY GAGES

PV1

PV2

PV3
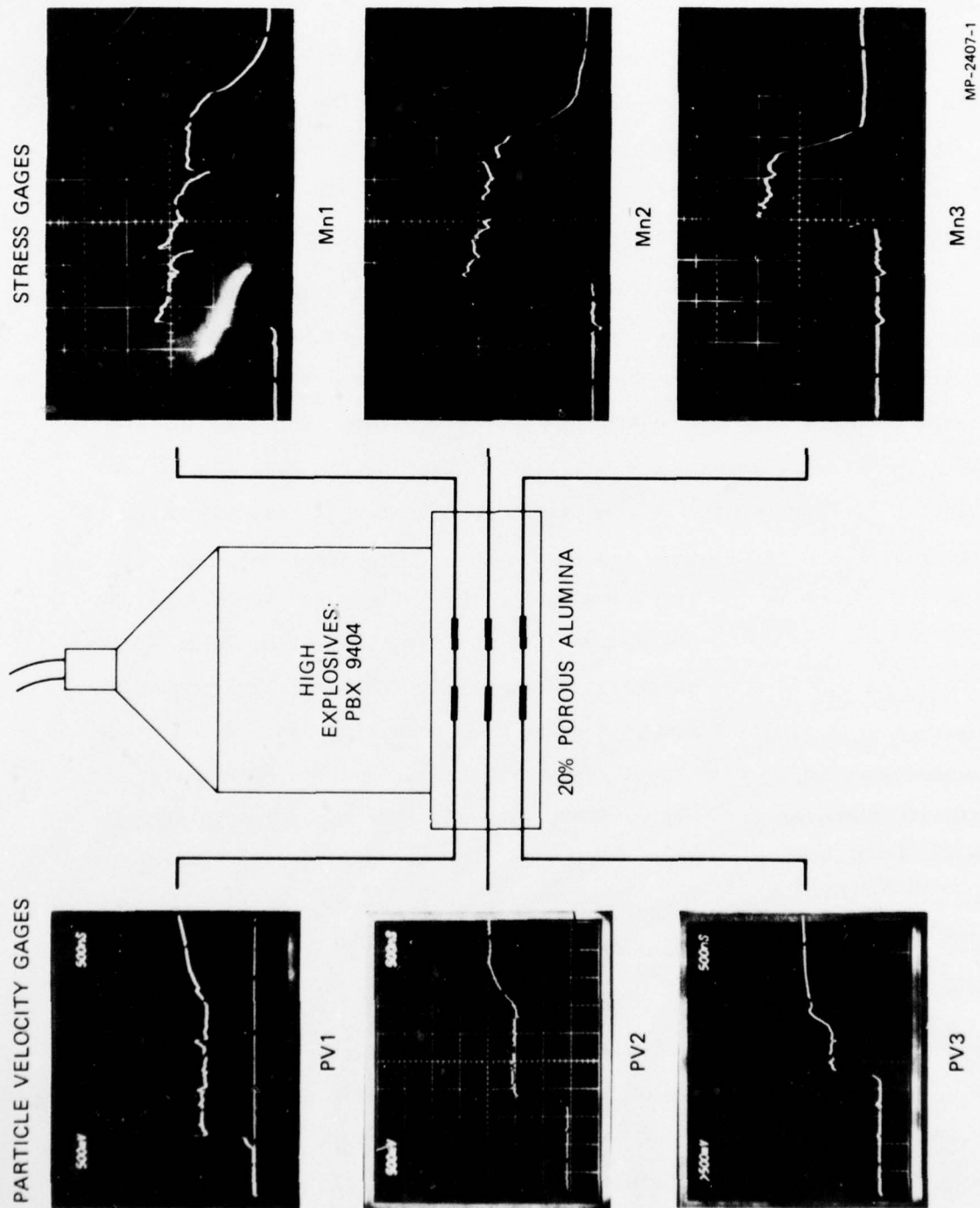
FIGURE 6   OSCILLOGRAPHS FROM SHOT NO. 1

23

caused by stress loading. Also, the stress gages appear to be noisier than the particle velocity records--a common occurrence when used in porous materials.

The large blips that appear during the relatively flat portions of both the stress and the particle velocity records for gage planes 1 and 2 are not noise, but in fact are perturbations of the flow due to reflections from gage plans 2 and 3. Decreases in the gage package thickness reduced the magnitude of these perturbations in all subsequent shots.

To analyze the data, we must first digitize the records, using the appropriate calibration to transform from voltage to particle velocity or stress and then to correlate the times of arrival to yield the composite particle velocity and stress histories shown in Figure 7. The particle velocity gages are calibrated by knowing the gage length and magnetic field strength. The manganin gages are calibrated by using the piezoresistance coefficient for loading and a linear calibration from the peak resistance to the final resistance for unloading. Because of the wide range of accepted piezoresistance coefficients for manganin (between 0.0025 and 0.0029 ohms/ohm/kbar), the stress calibration is adjusted when possible by a simple Hugoniot-Rankine jump condition calculation using the shock velocity from the stress gage records and the peak particle velocity from the particle velocity records. The zero time in the composite histories is purely arbitrary. The composite histories are, in reality, two-dimensional representations of the curves in three-dimensional space, with the third dimension, the Lagrangian position, perpendicular to the plane of the paper.

The next step in the analysis is to form a series of paths in three-dimensional space, each path joining one point on each of the three curves. The paths are drawn joining similar features on each curve--for example, the peaks of the precursor, the peaks of the main wave, the beginning of the unloading wave, and so on. Along the paths, the

24
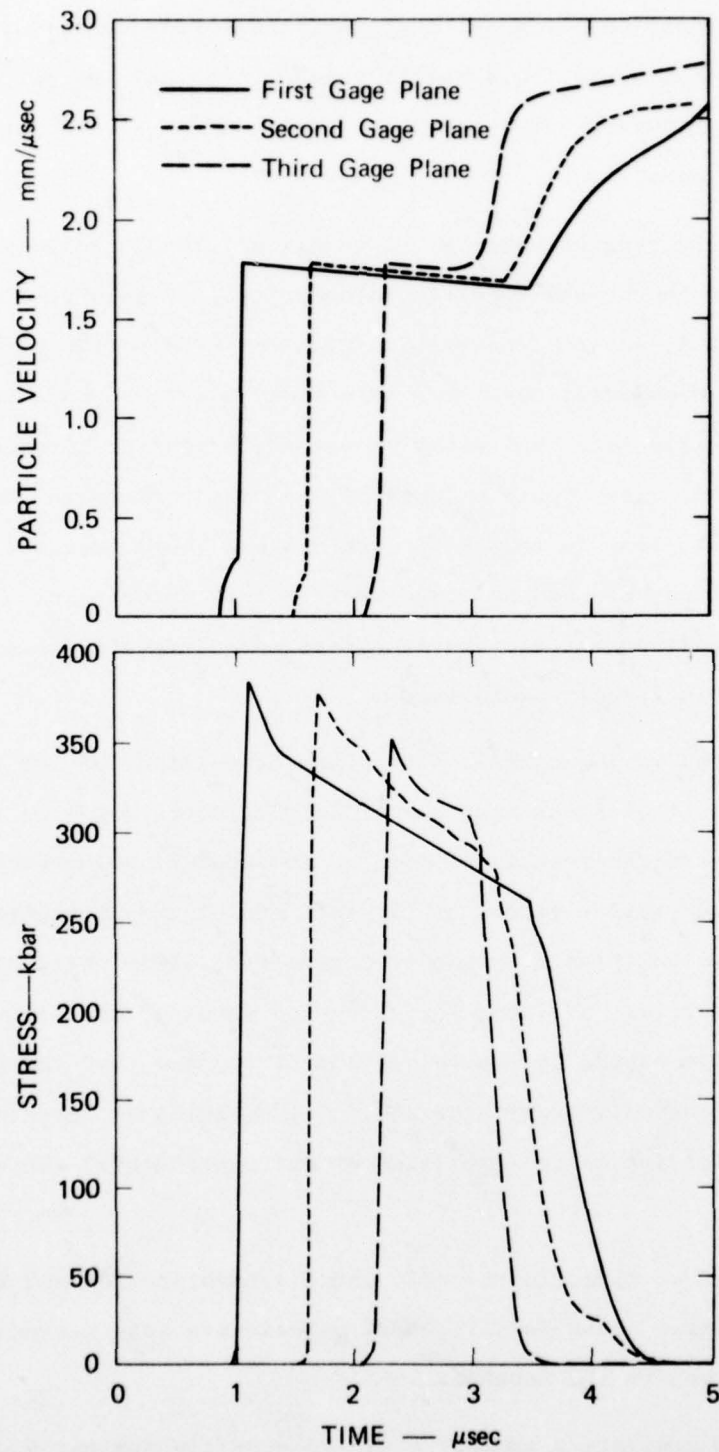
FIGURE 7   COMPOSITE PARTICLE VELOCITY AND STRESS HISTORIES FROM SHOT NO. 1

25

differential equations of mass, momentum, and energy conservation are integrated to calculate the specific volume, internal energy, and other constitutive parameters of interest. Details of this calculation are found in Reference 10.

When the Lagrangian analysis is completed, the constitutive paths are plotted in the stress-specific volume plane. Figure 8 is such a graph for Shot 1, showing the results from both the particle velocity and the stress gage calculations. For this shot, all three gage planes load up and down nearly identical paths except for slight differences in the position of the release path because of the slight decay in the peak stress from the first to the third gage planes. This indicates that time-dependent effects are not important in this material at this peak pressure (time-dependent yield effects are not noticeable here because the precursor is largely overdriven).

Figure 9 shows the constitutive paths calculated for the first gage plane from both the stress and the particle velocity gages on the same graph, to compare the results of the two independent measurements. The paths are quite similar except at the tail end of the unloading, where the particle velocity data appear to degenerate. This could be caused by either the arrival of lateral rarefaction waves or the arrival of a compressive wave caused by the reflection of the front of the rarefaction wave from the explosive gas interface. The differences between the paths give some indication of the precision of our experimental and analytical technique.

The digitized particle velocity and stress histories and the calculated constitutive paths for all those experiments that yielded analyzable records are given in the Appendix.

Figure 10 presents a composite of the constitutive paths calculated from all the analyzable sintered alumina experiments. The curve shown
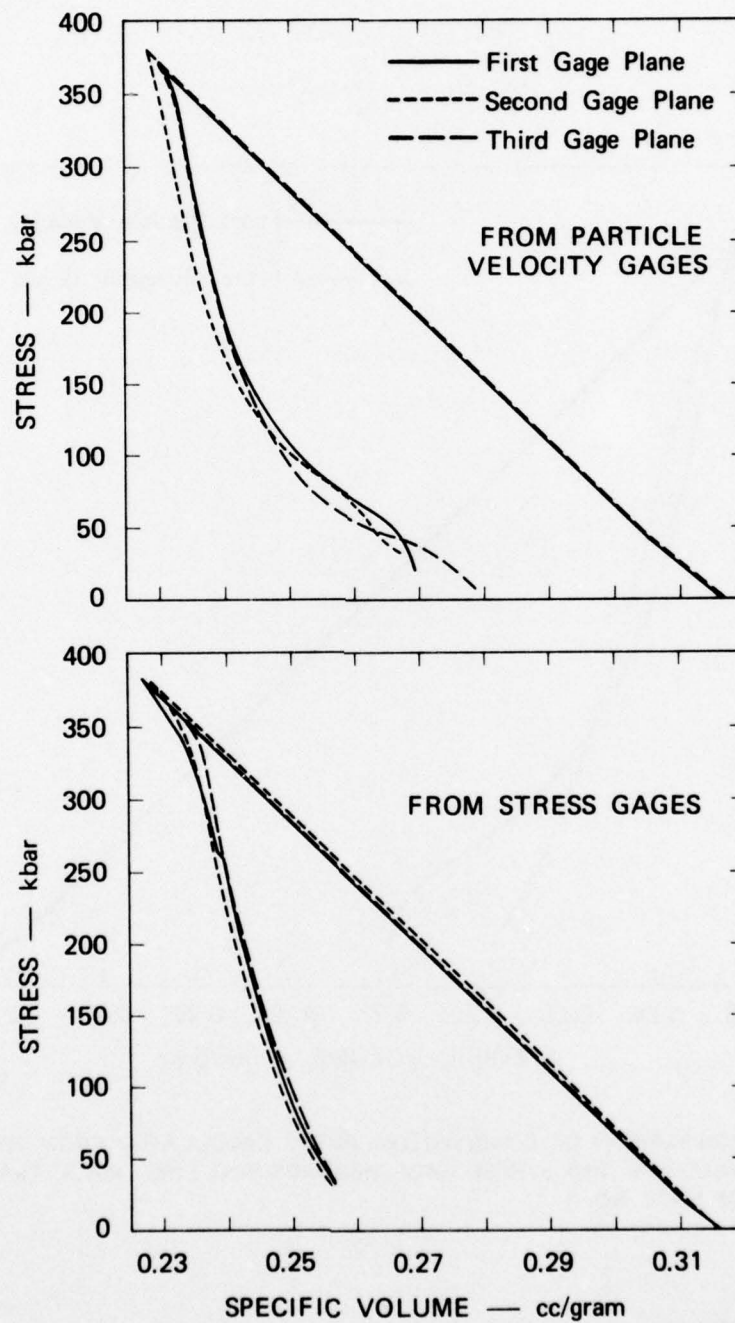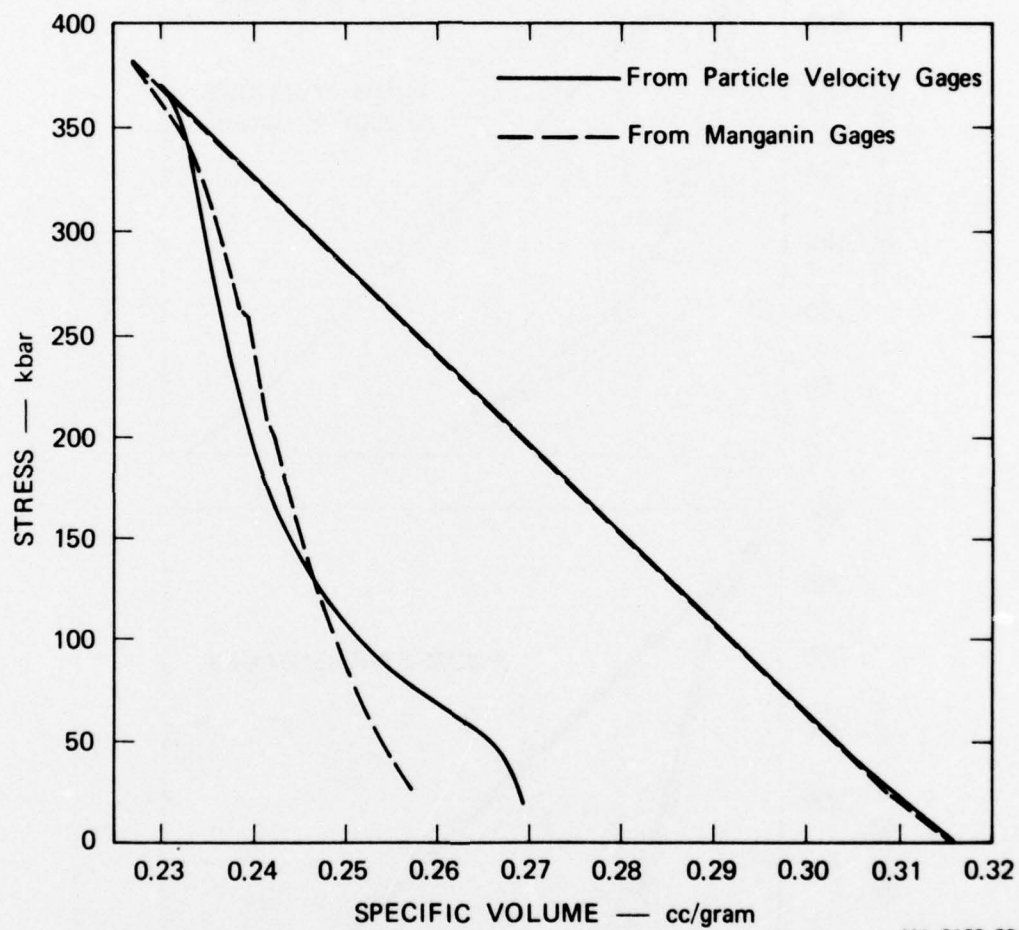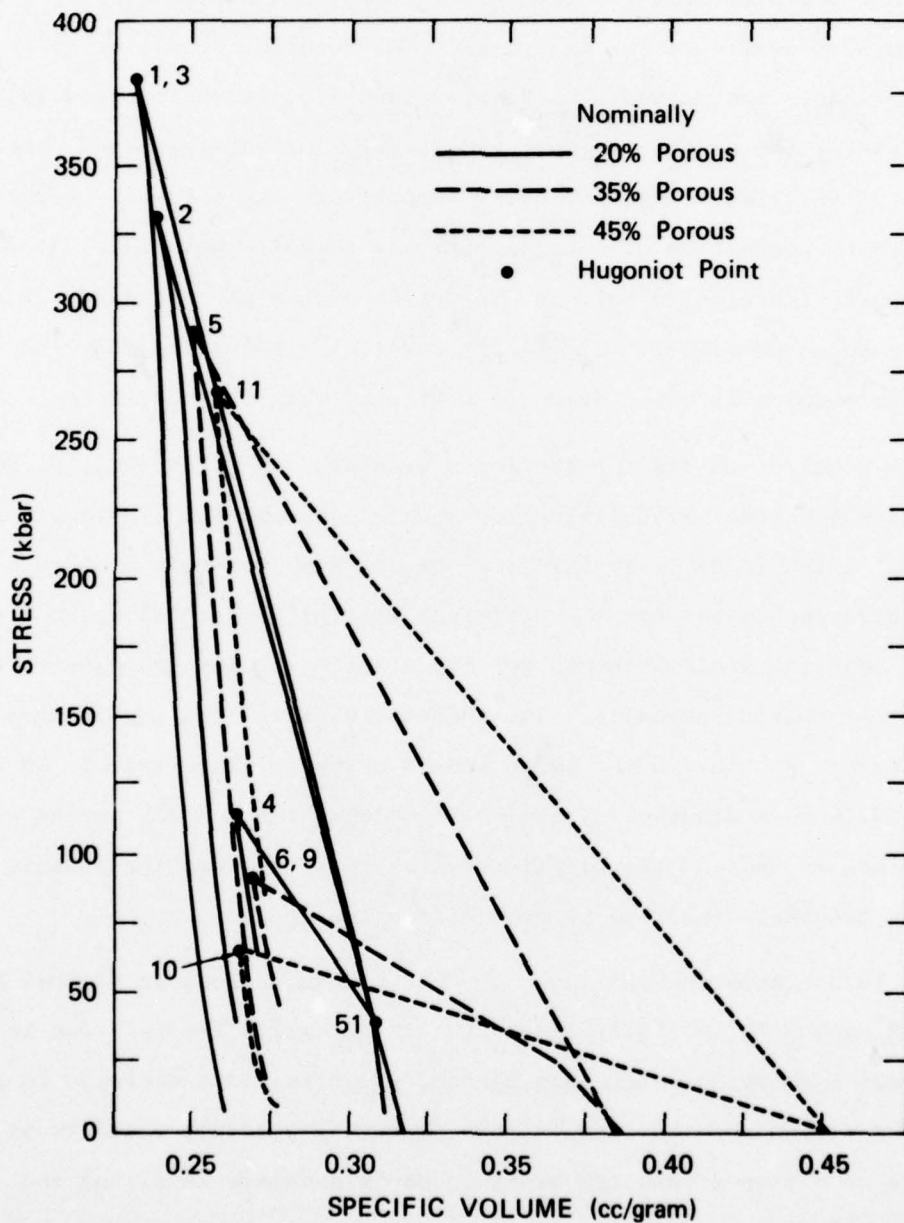
26

FIGURE 8   STRESS-VOLUME CONSTITUTIVE PATHS CALCULATED FOR SHOT NO. 1

27

FIGURE 9   COMPARISON OF CONSTITUTIVE PATHS CALCULATED FROM PARTICLE
VELOCITY AND STRESS GAGE RECORDS FOR FIRST GAGE PLANE
OF SHOT NO. 1

FIGURE 10 CONSTITUTIVE PATHS CALCULATED FROM SINTERED ALUMINA
EXPERIMENTS (NUMBERS REFER TO SHOT NUMBER)

MA-3163-85

for each shot is an average of the constitutive paths at the middle gage location calculated from the particle velocity and stress gage record (if both were available for analysis). The Hugoniot points of the higher pressure shots (Shots 1, 2, 3, 5, and 11), which involved full compaction of the porous alumina, are slightly offset from each other because of the higher Hugoniot point temperature and internal energies generated by compaction of a higher initial porosity material. Also in these shots, the elastic wave is overdriven by the plastic wave. Finally, the release paths are all very nearly parallel, indicating that the unloading modulus is not a strong function of the internal energy.

The Hugoniot points for the lower pressure shots (Shots 4, 6, 9, and 10), which also probably involve complete compaction, are very nearly colinear, which is not surprising, since the Hugoniot point internal energy differences between the different initial porosities are not very large. Both the yield strength and the elastic modulus decrease as a function of initial porosity. The Hugoniot elastic limit drops from approximately 43 kbar in the 20% porous alumina to approximately 30 kbar in the 35% porous alumina. The elastic modulus for the 45% porous alumina is so close to that of the plastic modulus that the Hugoniot elastic limit for that material cannot be perceived from the data.

It is not apparent in Figure 10, but it can be seen in Figures A-5, A-6, A-9, and A-10 in the Appendix that the constitutive relation in the yield region shows some time-dependence, resulting in a decrease in peak precursor stress and increase in peak precursor particle velocity as a function of distance into the alumina, and a decrease in stress and particle velocity immediately after the precursor. This quite complex behavior appears in Shots 4, 6, and 9 (it is beyond the scope of this paper to explain its phenomenology).

The results of the two gas gun shots (Shots 151 and 152) using

30

flame-sprayed alumina and flame-sprayed hafnium titanate are also presented in the Appendix. The calculated constitutive paths show the loading and unloading behavior in the region below 10 kbar.

IV REFERENCES

1. C. F. Petersen, W. J. Murri, and R. W. Gates, "Dynamic Properties of Rocks," SRI Final Report, for Defense Atomic Support Agency, DASA 2298, June 1969.

2. C. F. Petersen, W. J. Murri, and M. Cowperthwaite, "Hugoniot and Release-Adiabat Measurements for Selected Geologic Materials," J. Geophys. Res. 75, 2063-2072 (1970).

3. J. T. Rosenberg, "Dynamic Shear Strength of Shock-Loaded Granite and Polycrystalline Quartz," SRI Final Report, for Defense Nuclear Agency, DASA 2718, February 1971.

4. C. F. Petersen and D. C. Erlich, "Dynamic Properties of Rock Required for Prediction Calculations," SRI Final Report, for Defense Advanced Research Projects Agency, DARPA 1317, October 1972.

5. D. C. Erlich, D. C. Wooten, and R. C. Crewdson, "Dynamic Tensile Failure of Glycerol," J. Appl. Phys. 42, 5495-5502 (1971).

6. L. Seaman, R. F. Williams, J. T. Rosenberg, D. C. Erlich, and R. K. Linde, "Classification of Materials by Shock Properties," SRI Final Report, for Defense Nuclear Agency, DNA 2742F, October 1971.

7. R. F. Bourque, H. E. Lindberg, and D. C. Erlich, "Scale Model Underground Testing in Diamond Sculls," SRI Bimonthly Progress Report No. 4, for Defense Nuclear Agency, Contract DNA001-72-C-0027, 1973.

8. R. Fowles and R. F. Williams, "Plane Stress Wave Propagation in Solids," J. Appl. Phys. 41, 360-363 (1970).

9. M. Cowperthwaite and R. F. Williams, "Determination of Constitutive Relationships with Multiple Gages in Nondivergent Waves," J. Appl. Phys. 42, 456-462 (1971).

10. L. Seaman, "Lagrangian Analysis for Multiple Stress or Velocity Gages in Attenuating Waves," J. Appl. Phys. 45, 4303-4314 (1974).

11. M. J. Ginsberg, D. E. Grady, P. S. De Carli, and J. T. Rosenberg, "Effects of Stress on the Electrical Resistance of Ytterbium and Calibration of Ytterbium Stress Transducers," SRI Final Report, for Defense Nuclear Agency, DNA 3577F, August 1973.

12. D. D. Keough, "Procedure for Fabrication and Operation of Manganin Shock Pressure Gages," SRI Final Report, for Air Force Weapons Laboratory, AFWL-TR-68-57, August 1968.

Appendix

EXPERIMENTAL AND ANALYTICAL RECORDS AND
DISCUSSION OF EXPERIMENTAL PROBLEMS ENCOUNTERED

In this section are presented the experimental and analytical records for all the analyzable shots except for those for Shot 1, which were included in the main part of the report. Figures A-1—A-16 present the digitized composite particle velocity or stress gage records and the stress-volume constitutive paths calculated from these records. In each figure, the solid line represents the first gage plane, the short-dashed line represents the second gage plane, and the long-dashed line represents the third gage plane. The distances between the various gage planes and other shot parameters are shown in Tables 1 and 2 in the report.

Shots 2, 3, 4, 5, and 10 include data from both particle velocity and stress records, Shots 11 and 151 include only particle velocity data, and Shots 151 and 152 include only stress gage data. Finally, the particle velocity data from Shot 6 are shown together with the stress data from Shot 9, because these shots are identical as to type of explosive used and peak pressure attained.

In some cases, only the loading portion of the particle velocity or stress records and the calculated constitutive path during loading are shown, because the unloading portion of the gage records was not amenable to Lagrangian analysis. Some records or portions of records were not analyzable, for several reasons:

(1) The stress gages partially shorted out at high pressures because of increased conductivity of the encapsulants. This was particularly true with the higher porosity alumina, which reached higher temperatures on loading. (Shots 8 and 11)

A-1

(2) The signal-to-noise ratio was too small. This was the case with the HE shots on the flame-sprayed alumina, although the cause of the excessive noise is not clearly known.

(3) In Shot 8, the particle velocity records appeared to be excellent, but because of a short through one or more of the adjoining wires in the Helmholtz coils, the current through the coils and hence, the magnetic field, was unknown.

(4) In the gas gun shot with sintered alumina (Shot 51), the peak stress was apparently above that of the phase change of ytterbium,[11] so the ytterbium gage records were meaningless.

(5) The features of the unloading portions of the records at the different gage planes were dissimilar enough so that it was difficult to draw paths through the different records joining points along which the differential equations could be integrated. Gage planes could be placed closer together to alleviate this problem.
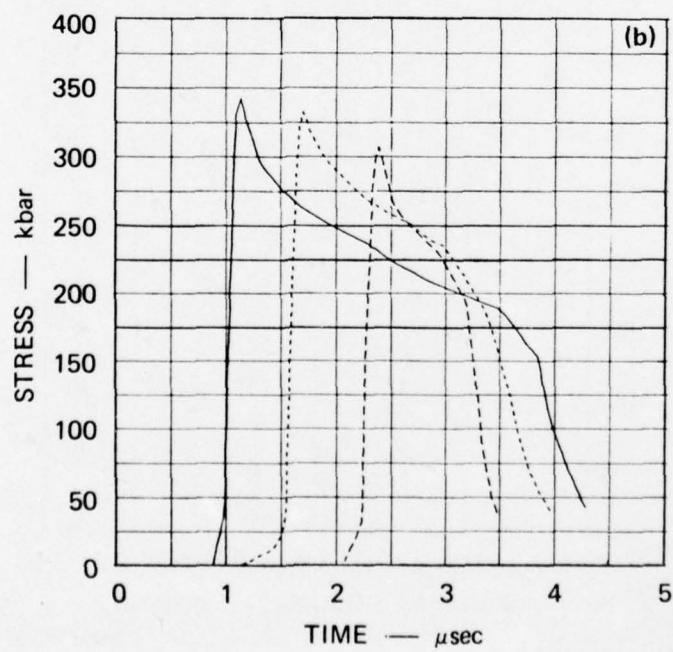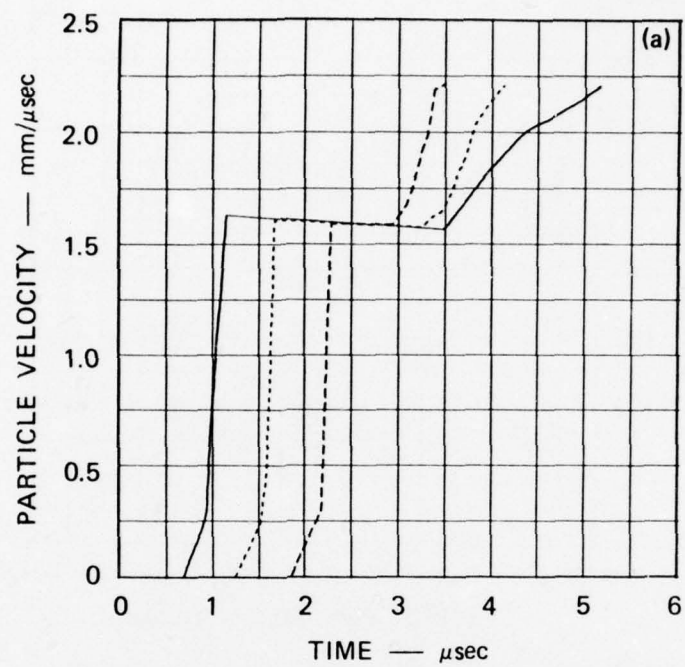
FIGURE A-1   COMPOSITE (a) PARTICLE VELOCITY HISTORIES AND
(b) STRESS HISTORIES FROM SHOT NO. 2
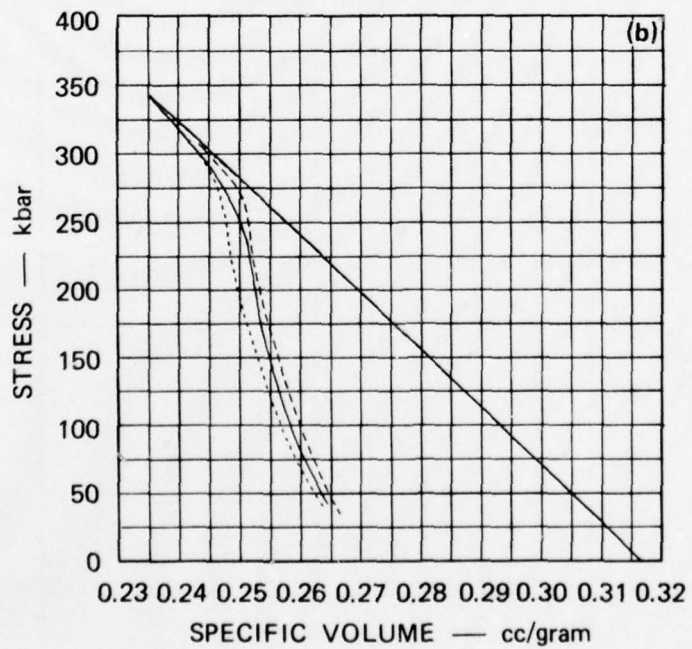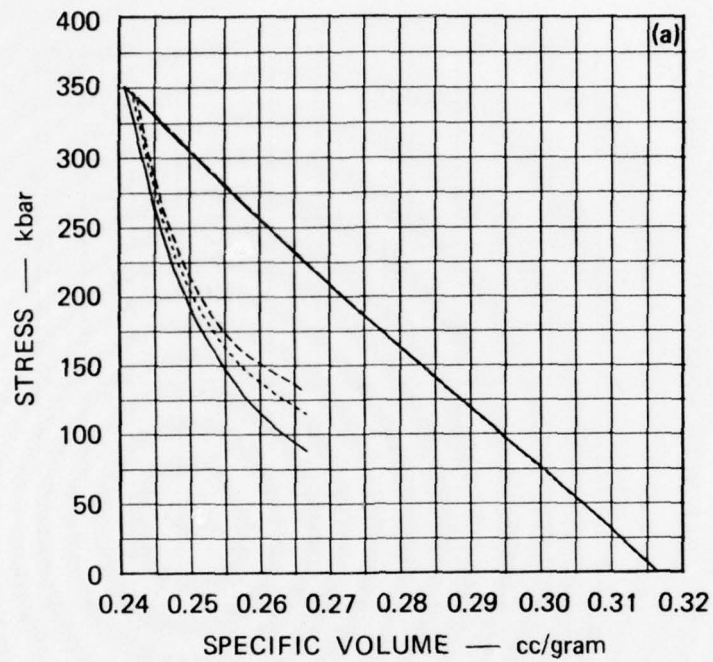
FIGURE A-2   CONSTITUTIVE PATHS CALCULATED FROM
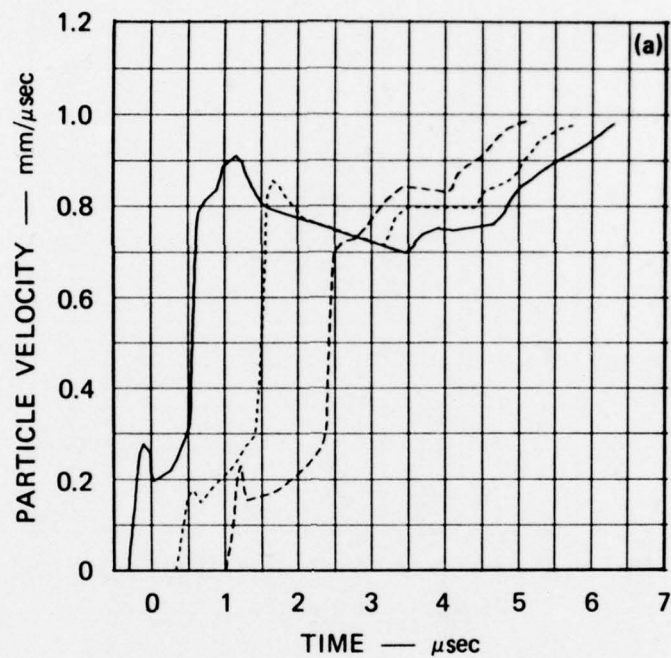(a) PARTICLE VELOCITY GAGE AND
(b) STRESS GAGE RECORDS FOR SHOT NO. 2
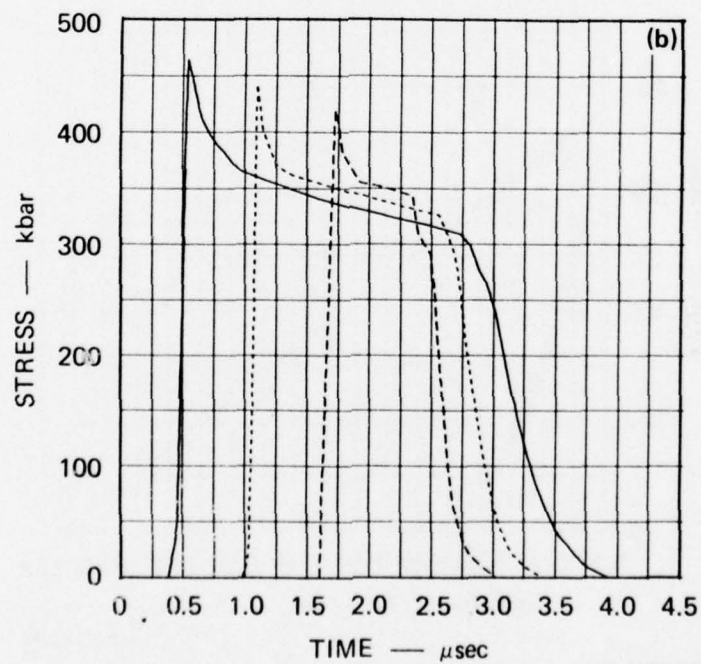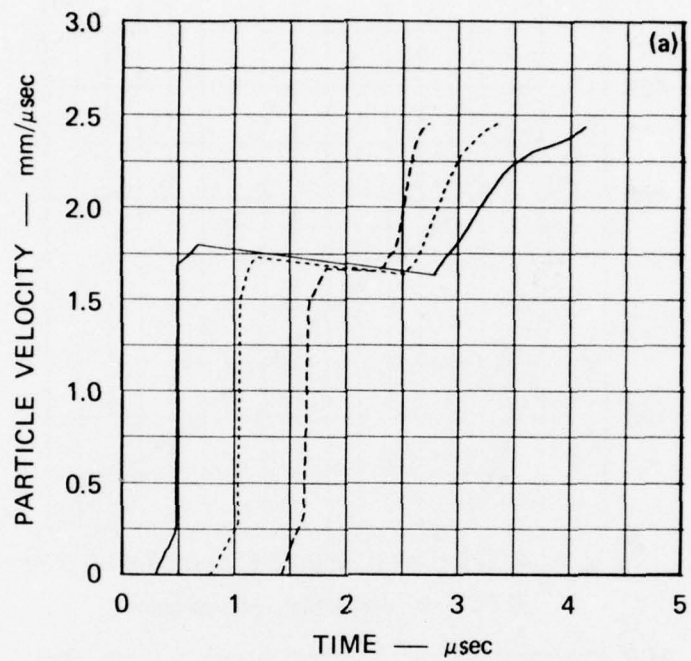
FIGURE A-3   COMPOSITE (a) PARTICLE VELOCITY HISTORIES AND
(b) STRESS HISTORIES FROM SHOT NO. 3

MA-3163-71
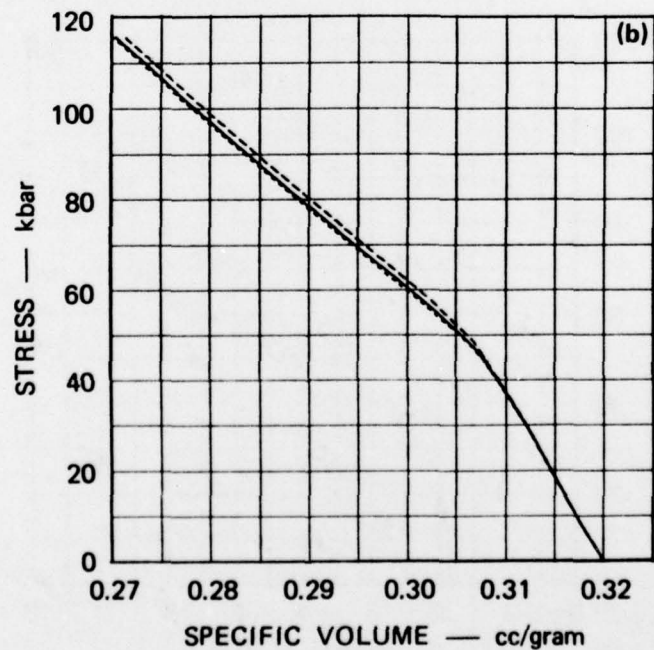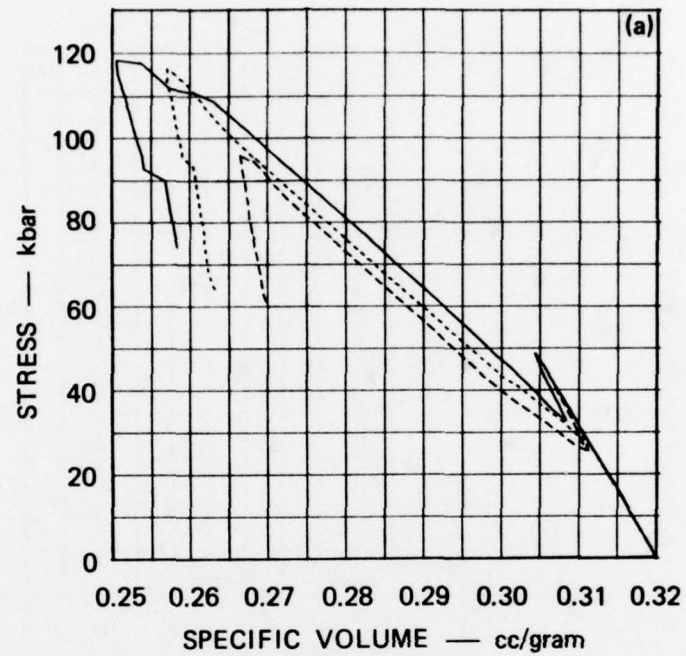
A-5
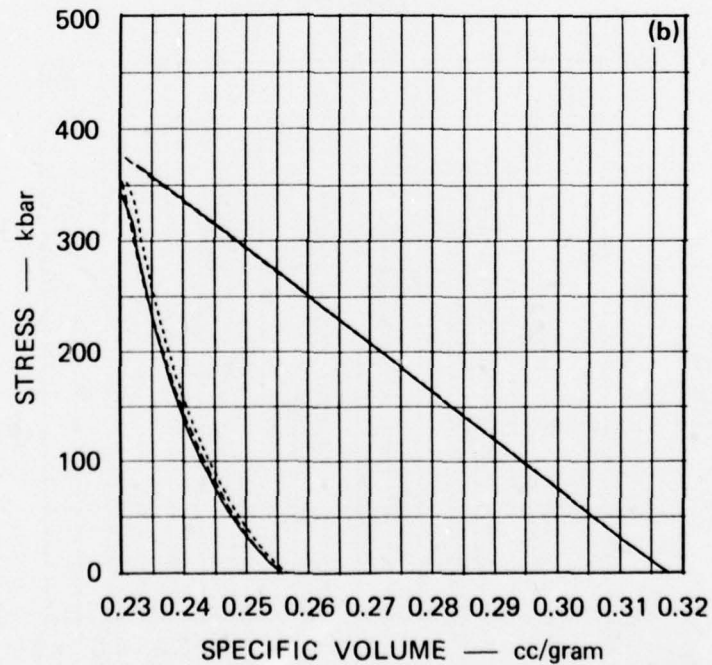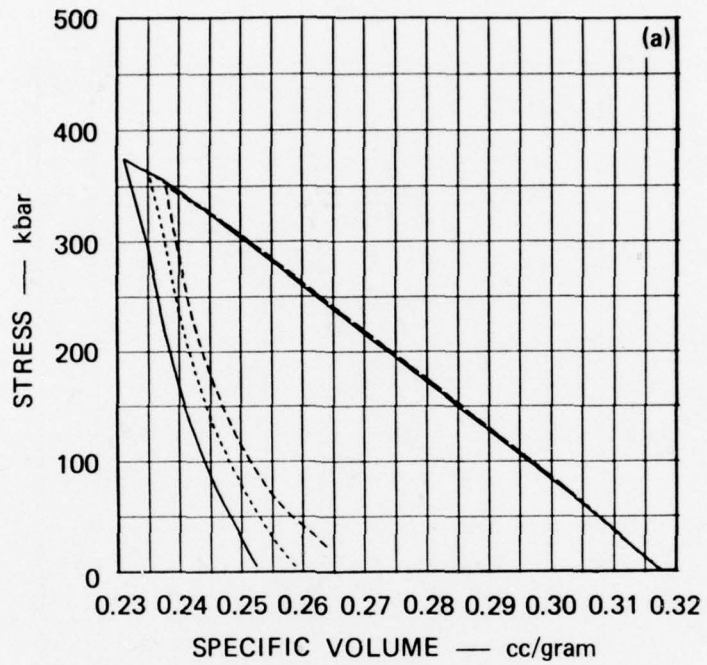
FIGURE A-4   CONSTITUTIVE PATHS CALCULATED FROM
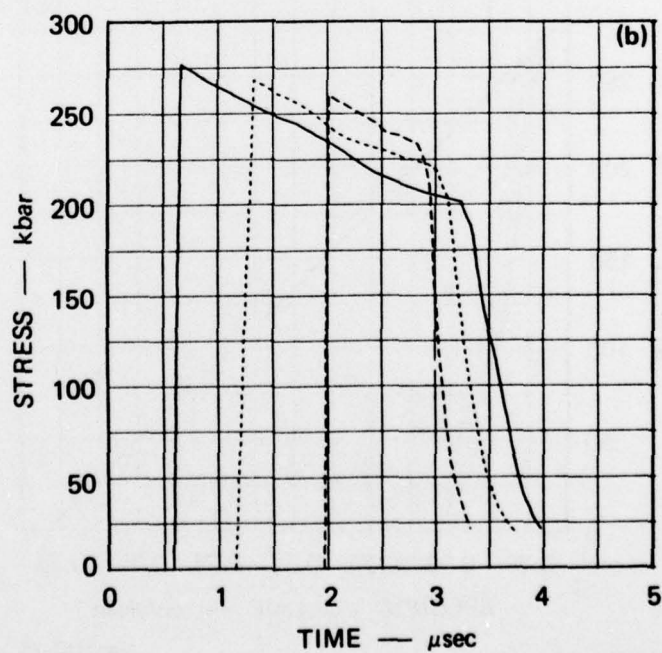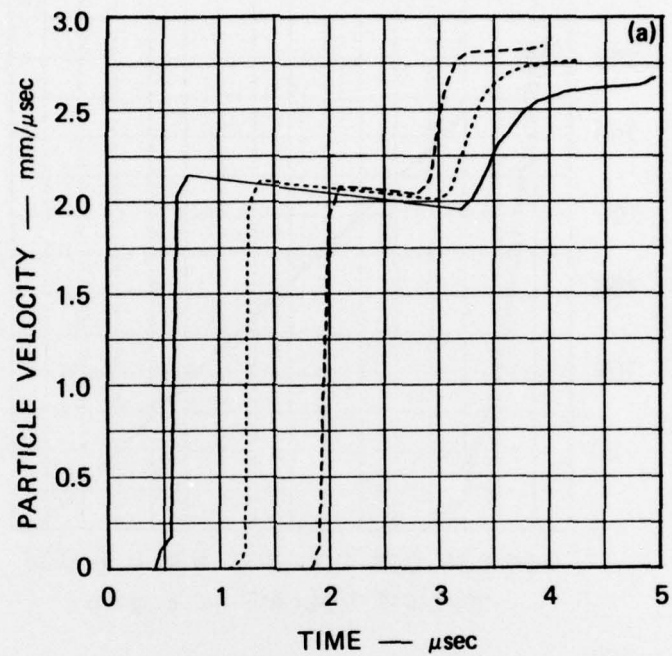(a) PARTICLE VELOCITY GAGE AND
(b) STRESS GAGE RECORDS FOR SHOT NO. 3
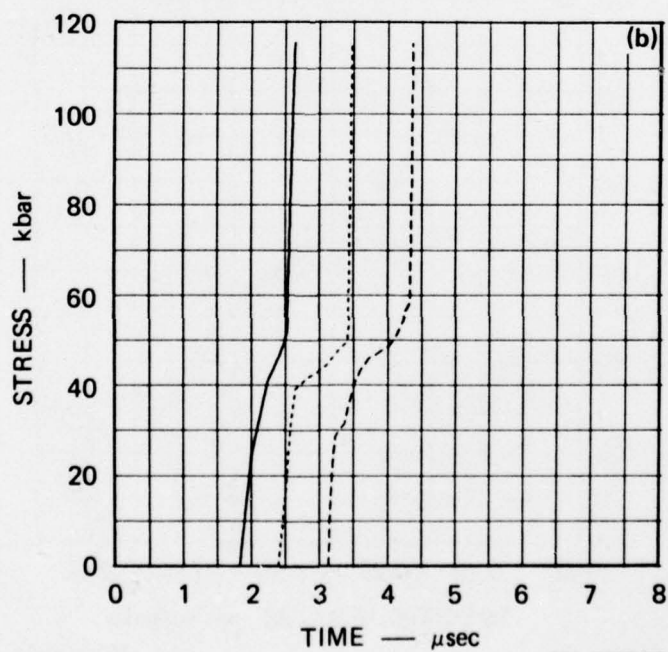
FIGURE A-5   COMPOSITE (a) PARTICLE VELOCITY HISTORIES AND
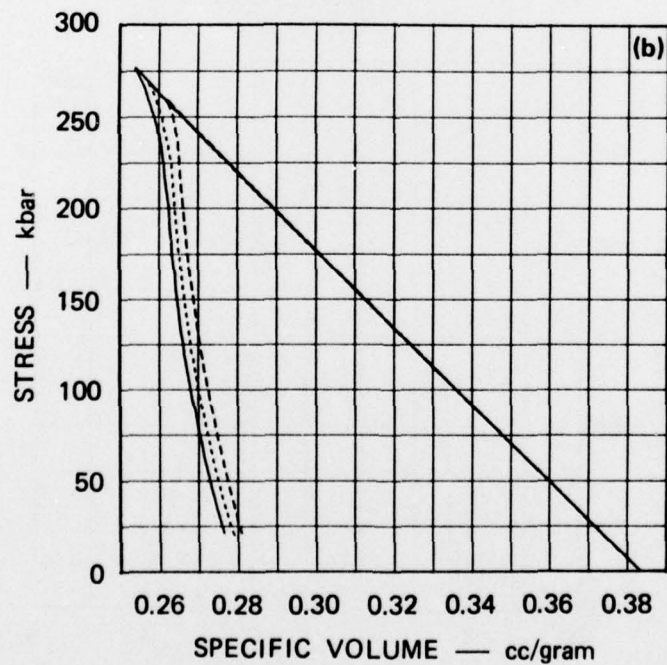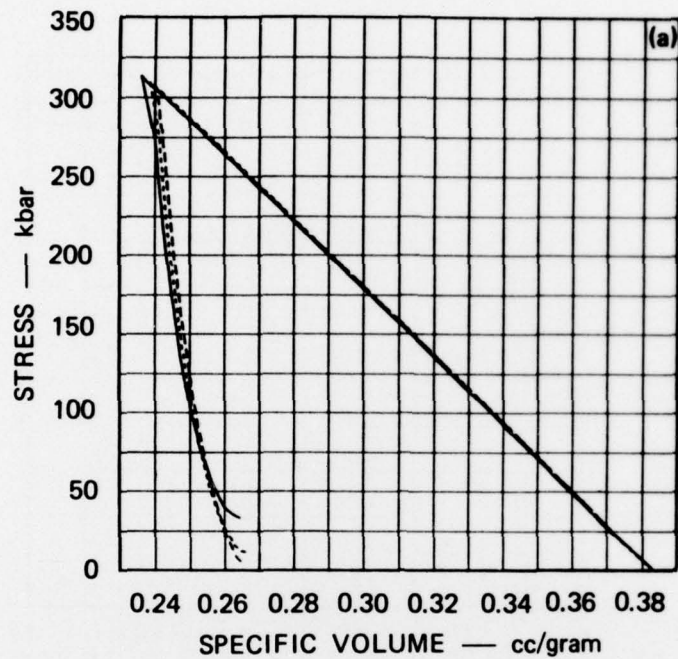(b) STRESS HISTORIES FROM SHOT NO. 4

FIGURE A-6 CONSTITUTIVE PATHS CALCULATED FROM
(a) PARTICLE VELOCITY GAGE AND
(b) STRESS GAGE RECORDS FOR SHOT NO. 4

MA-3163-74

FIGURE A-7   COMPOSITE (a) PARTICLE VELOCITY HISTORIES AND
(b) STRESS HISTORIES FROM SHOT NO. 5

MA-3163-75

FIGURE A-8 CONSTITUTIVE PATHS CALCULATED FROM
(a) PARTICLE VELOCITY GAGE AND
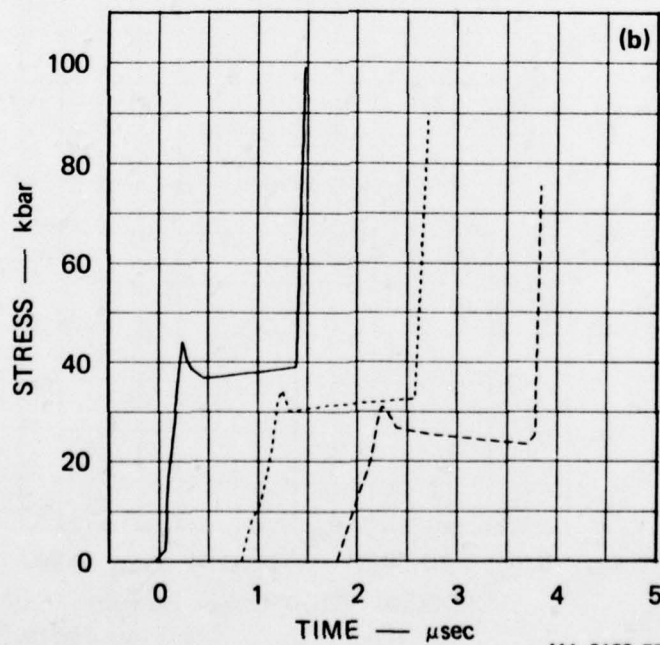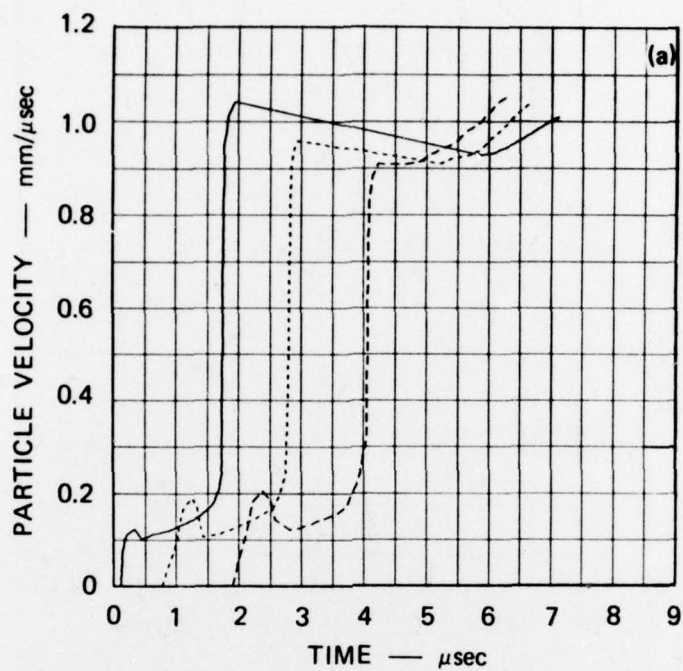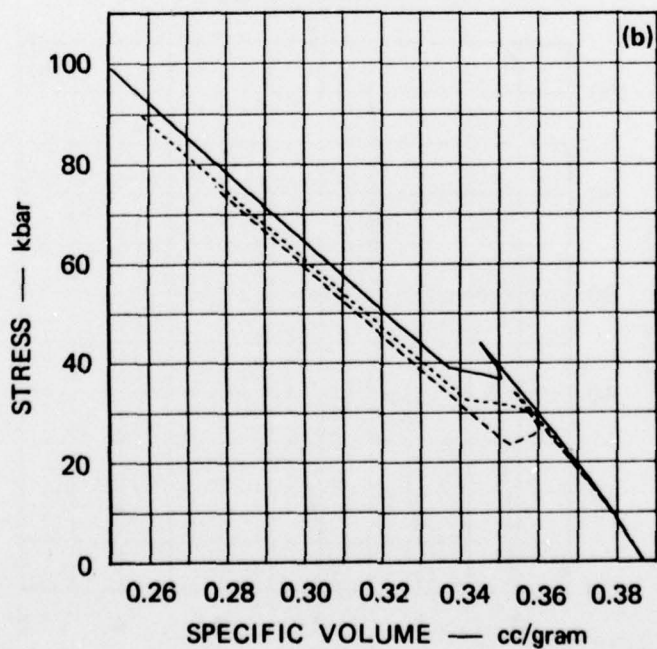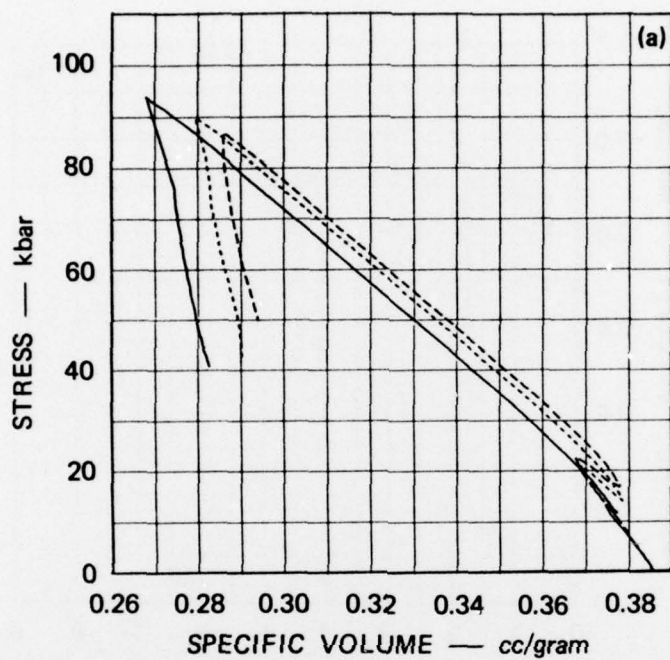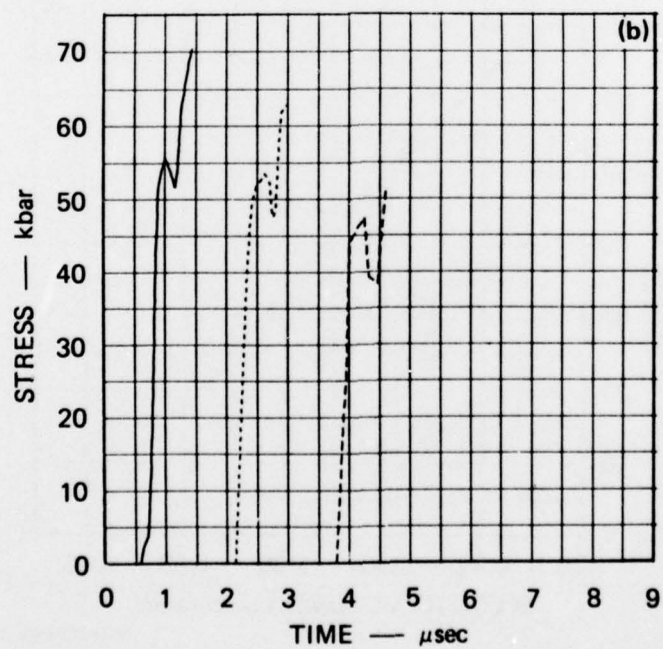(b) STRESS GAGE RECORDS FOR SHOT NO. 5

MA-3163-76

FIGURE A-9   COMPOSITE (a) PARTICLE VELOCITY HISTORIES FROM
SHOT NO. 6 AND (b) STRESS HISTORIES FROM
SHOT NO. 9

MA-3163-77

FIGURE A-10 CONSTITUTIVE PATHS CALCULATED FROM
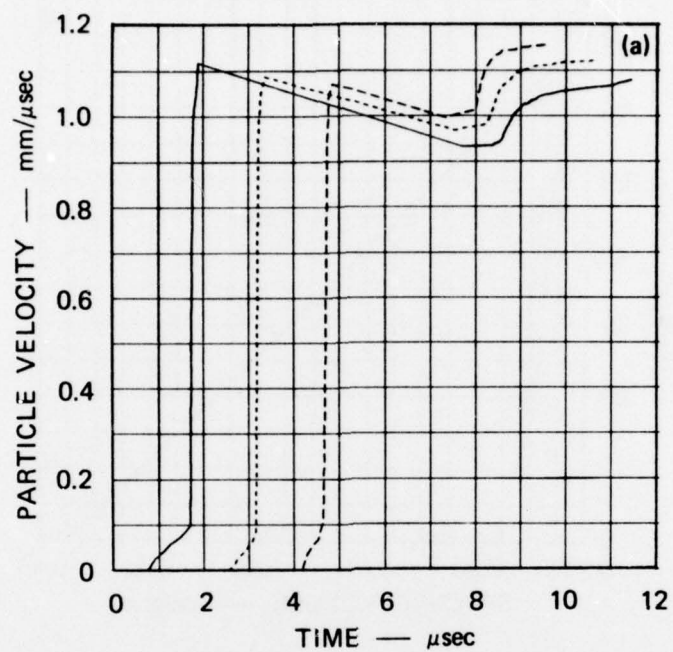(a) PARTICLE VELOCITY GAGE FOR SHOT NO. 6 AND
(b) STRESS GAGE RECORDS FOR SHOT NO. 9

MA-3163-78

FIGURE A-11   COMPOSITE (a) PARTICLE VELOCITY HISTORIES AND
(b) STRESS HISTORIES FROM SHOT NO. 10
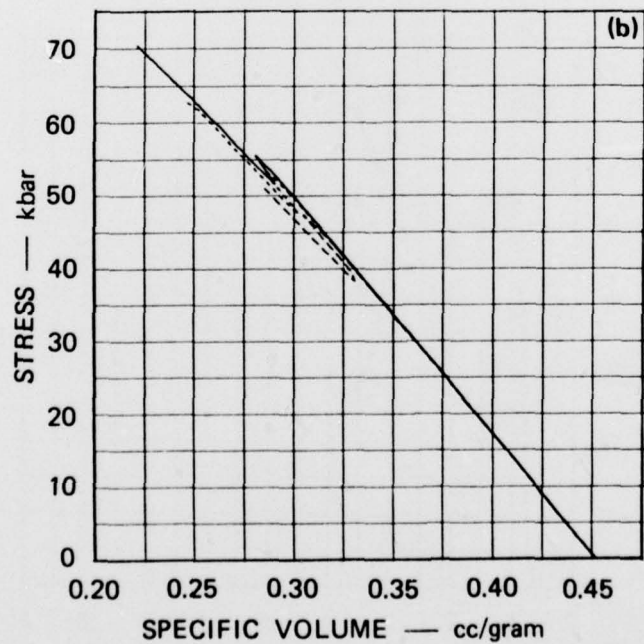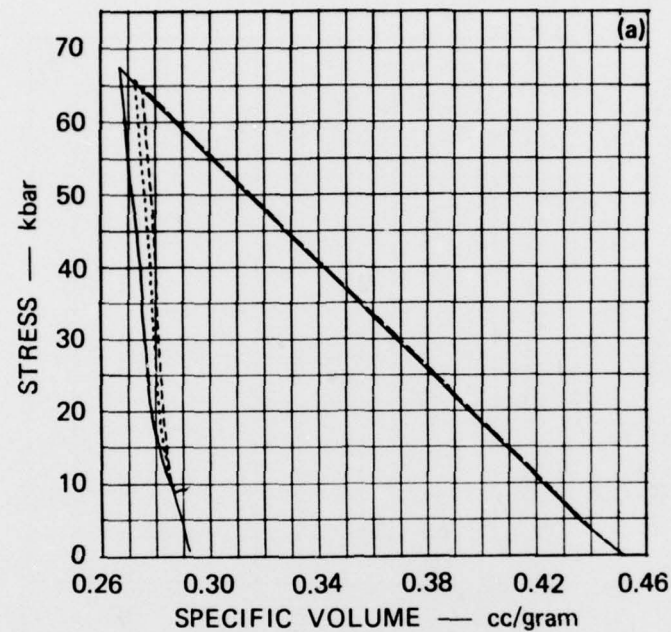
MA-3163-79

FIGURE A-12   CONSTITUTIVE PATHS CALCULATED FROM
(a) PARTICLE VELOCITY GAGE AND
(b) STRESS GAGE RECORDS FOR SHOT NO. 10
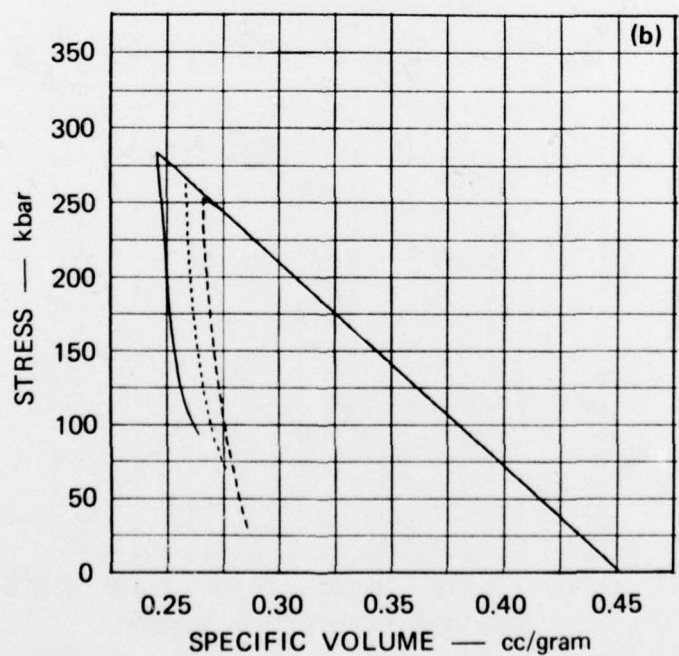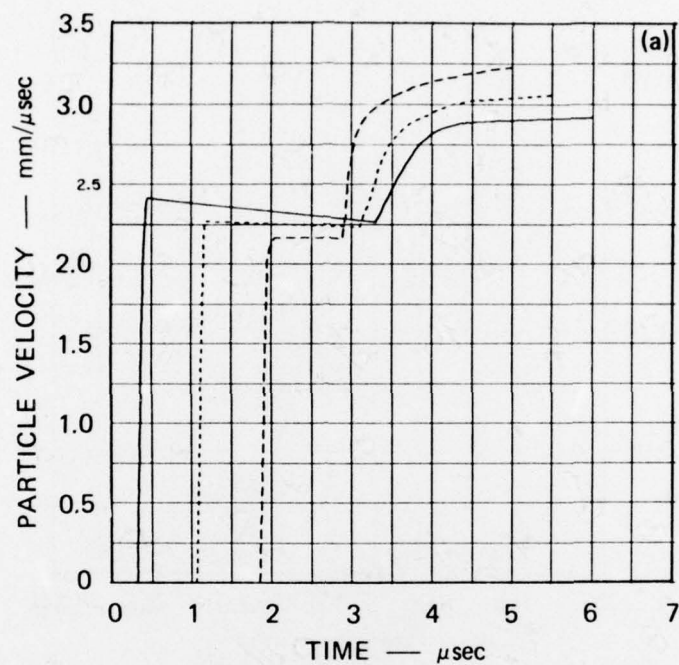
FIGURE A-13   COMPOSITE PARTICLE VELOCITY HISTORIES (a)
AND CALCULATED CONSTITUTIVE PATHS (b)
FROM SHOT NO. 11
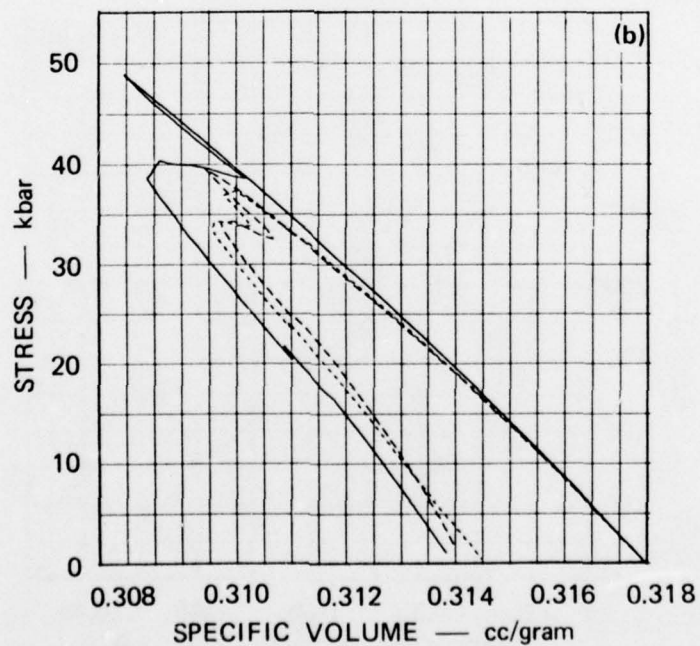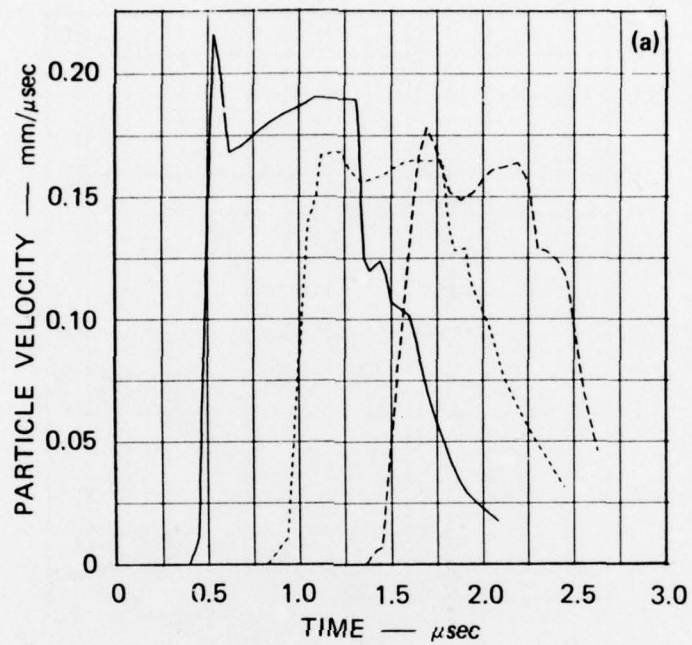
MA-3163-81

MA-3163-82

FIGURE A-14   COMPOSITE PARTICLE VELOCITY HISTORIES (a)
AND CALCULATED CONSTITUTIVE PATHS (b)
FROM SHOT NO. 51
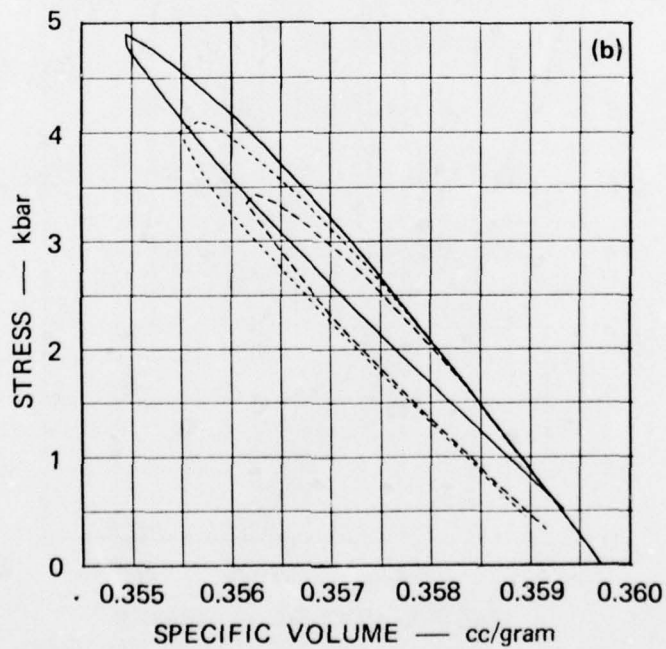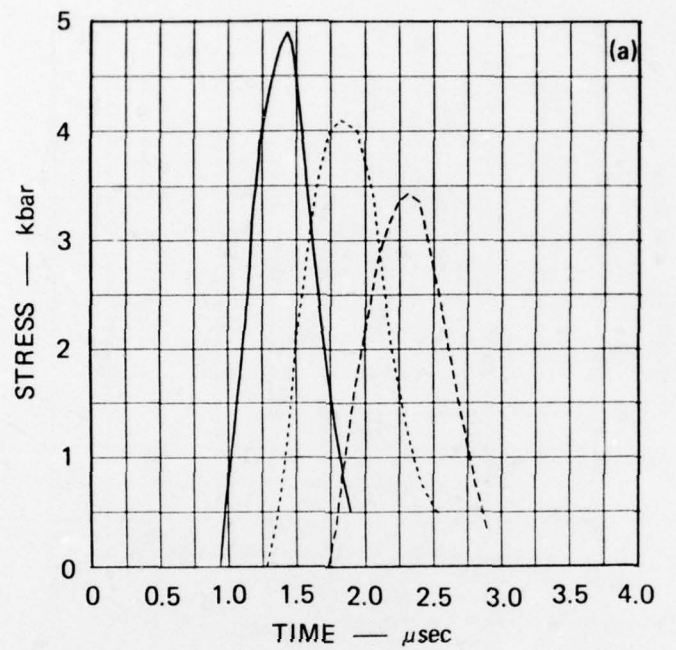
FIGURE A-15   COMPOSITE STRESS HISTORIES (a) AND
CALCULATED CONSTITUTIVE PATHS (b)
FROM SHOT NO. 151
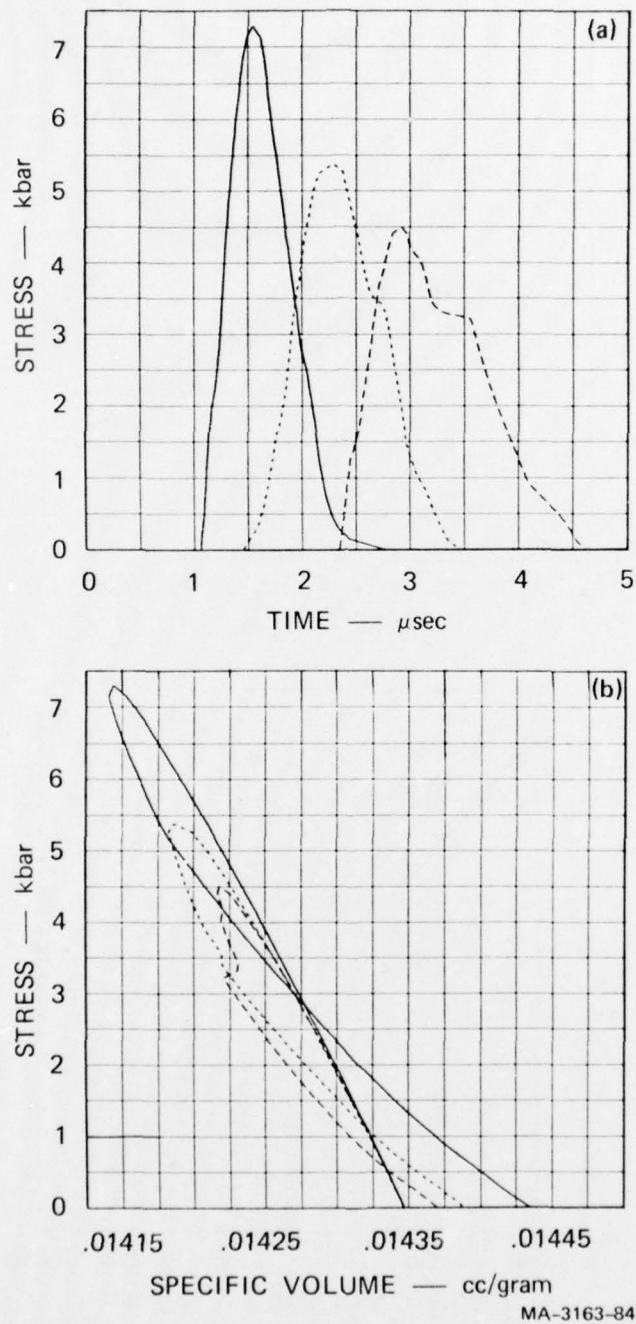
FIGURE A-16 COMPOSITE STRESS HISTORIES (a) AND
CALCULATED CONSTITUTIVE PATHS (b)
FROM SHOT NO. 152

A-18

DISTRIBUTION LIST

DEPARTMENT OF DEFENSE

Director
Defense Advanced Rsch. Proj. Agency
    ATTN: Strategic Tech. Office

Director
Defense Communications Agency
    ATTN: NMCSSC, Code 510

Defense Documentation Center
Cameron Station
12 cy ATTN: TC

Director
Defense Intelligence Agency
    ATTN: DT-1C, Nuc. Eng. Branch
    ATTN: DT-2, Wpns. and Sys. Div.
    ATTN: DI-7D

Director
Defense Nuclear Agency
    ATTN: SPAS
    ATTN: STSP
    ATTN: DDST
    ATTN: TISI, Archives
3 cy ATTN: TITL, Tech. Library

Under Secretary of Def. for Rsch. & Engrg.
    ATTN: S&SS (OS)

Commander
Field Command
Defense Nuclear Agency
    ATTN: FCPR
    ATTN: FCTMD
    ATTN: FCTMOF

Director
Joint Strat. Tgt. Planning Staff, JCS
    ATTN: JPTP
    ATTN: JLTW-2
    ATTN: JPTM

Chief
Livermore Division Fld. Command, DNA
Lawrence Livermore Laboratory
    ATTN: FCPRL

OJCS/J-5
    ATTN: J-5, Plans & Policy, Nuc. Div.

Defense Communication Engr. Ctr.
    ATTN: Code 720, John Worthington

DEPARTMENT OF THE ARMY

Program Manager
BMD Program Office
    ATTN: DACS-BMT, Clifford E. McLain
    ATTN: DACS-BMT, John Shea
    ATTN: DACS-BMZ-D, Julian Davidson
    ATTN: DACS-BMZ

Dep. Chief of Staff for Rsch. Dev. & Acq.
    ATTN: NCB Division

DEPARTMENT OF THE ARMY

Commander
BMD System Command
    ATTN: BDMSC-TEN, Noah J. Hurst

Deputy Chief of Staff for Ops. & Plans
    ATTN: Dir. of Nuc. Plans & Policy

Commander
Harry Diamond Laboratories
    ATTN: DRXDO-RBH, James H. Gwaltney
    ATTN: DRXDO-TF, Robert B. Oswald, Jr.
    ATTN: DRXDO-NP

Commander
Picatinny Arsenal
    ATTN: SARPA-FR-E, Louis Avrami
    ATTN: SMUPA-MD, Henry Opat
    ATTN: SARPA-ND-C-T, Donald Miller

Director
Trasana
    ATTN: R. E. DeKinder, Jr.

Director
U.S. Army Ballistic Research Labs.
    ATTN: DRXRD-BVL, William J. Schuman, Jr.
    ATTN: DRXBR-TB, J. T. Frasier
    ATTN: Robert E. Eichelberger

Commander
U.S. Army Mat. & Mechanics Rsch. Ctr.
    ATTN: DRXMR-HH, John F. Dignam

Commander
U.S. Army Materiel Dev. & Readiness Cmd.
    ATTN: DRCDE-D, Lawrence Flynn

Commander
U.S. Army Missile Command
    ATTN: DRSMI-RRR, Bud Gibson
    ATTN: DRS-RKP, W. B. Thomas
    ATTN: DRSMI-XS, Chief Scientist
    ATTN: DRCPM-PE-EA, Wallace O. Wagner

Commander
U.S. Army Nuclear Agency
    ATTN: ATCA-NAW

DEPARTMENT OF THE NAVY

Chief of Naval Material
    ATTN: MAT 0323, Irving Jaffe

Chief of Naval Operations
    ATTN: OP 62
    ATTN: OP 981

Chief of Naval Research
    ATTN: Code 464, Thomas P. Quinn

Director
Naval Research Laboratory
    ATTN: Gerald Cooperstein, Code 7770
    ATTN: Mario A. Persechino, Code 5180
    ATTN: Tech. Library, Code 2600

DEPARTMENT OF THE NAVY (Continued)

Commander
Naval Sea Systems Command
        ATTN: 0333A, Marlin A. Kinna

Officer-In-Charge
Naval Surface Weapons Center
        ATTN: Code WA07, Carson Lyons
        ATTN: Code WA501, Navy Nuc. Prgms. Off.
        ATTN: Code 2302, Leo F. Gowen

Director
Strategic Systems Project Office
        ATTN: NSP-272, CDR Leslie Stoessl

DEPARTMENT OF THE AIR FORCE

AF Materials Laboratory, AFSC
        ATTN: MBC, Donald L. Schmidt
        ATTN: MAS
        ATTN: T. Nicholas

AF Rocket Propulsion Laboratory, AFSC
        ATTN: RTSN, G. A. Beale

AF Weapons Laboratory, AFSC
        ATTN: SUL
        ATTN: DYV
        ATTN: Dr. Minge
        ATTN: DYS, Lt E. J. Burns

Commander
Foreign Technology Division, AFSC
        ATTN: TDFBD, J. D. Pumphrey
        ATTN: TDPTN

Headquarters, USAF/RD
        ATTN: RDQSM
        ATTN: RDPM
        ATTN: RD
        ATTN: RDQ

SAMSO/DY
        ATTN: DYS

SAMSO/MN
        ATTN: MNNR

SAMSO/RS
        ATTN: RSS
        ATTN: RSSE

Commander In Chief
Strategic Air Command
        ATTN: DOXT
        ATTN: XPFS

DEPARTMENT OF ENERGY

Division of Military Application
        ATTN: Doc. Control for Res. & Dev. Branch
        ATTN: Doc. Control for LTC D. L. McNutt
        ATTN: Doc. Control for CDR R. E. Peterson

DEPARTMENT OF ENERGY (Continued)

University of California
Lawrence Livermore Laboratory
        ATTN: G. Staihle, L-24
        ATTN: Joseph E. Keller, Jr., L-125
        ATTN: C. Joseph Taylor, L-92

Los Alamos Scientific Laboratory
        ATTN: Doc. Control for J. W. Taylor
        ATTN: Doc. Control for R. S. Thurston
        ATTN: Doc. Control for John McQueen

Sandia Laboratories
Livermore Laboratory
        ATTN: Doc. Control for 8131, H. F. Norris, Jr.
        ATTN: Doc. Control for T. Gold
        ATTN: Doc. Control for C. S. Hoyle

Sandia Laboratories
        ATTN: Doc. Control for R. R. Boade
        ATTN: Doc. Control for Albert Chabai
        ATTN: Doc. Control for D. McCloskey

DEPARTMENT OF DEFENSE CONTRACTORS

Aerospace Corporation
        ATTN: Richard Crolius, A2-RM1027
        ATTN: R. Allen

Avco Research & Systems Group
        ATTN: John Gilmore, J400
        ATTN: John E. Stevens, J100

Battelle Memorial Institute
        ATTN: Merwyn R. Vanderlind

The Boeing Company
        ATTN: Brian Lempriere

Brown Engineering Company, Inc.
        ATTN: Ronald Patrick

Effects Technology, Inc.
        ATTN: Robert Wengler

Ford Aerospace & Communications Operations
        ATTN: P. Spangler

General Electric Company
Space Division
Valley Forge Space Center
        ATTN: Phillip Cline
        ATTN: G. Harrison
        ATTN: Carl Anderson

General Electric Company
TEMPO-Center for Advanced Studies
        ATTN: DASIAC

Institute for Defense Analyses
        ATTN: Joel Bengston
        ATTN: IDA Librarian, Ruth S. Smith

DEPARTMENT OF DEFENSE CONTRACTORS (Continued)

ION Physics Corporation
    ATTN: Robert D. Evans

Kaman AviDyne
Division of Kaman Sciences Corp.
    ATTN: Norman P. Hobbs

Kaman Sciences Corporation
    ATTN: Thomas Meagher
    ATTN: Frank H. Shelton
    ATTN: John R. Hoffman
    ATTN: Albert P. Bridges
    ATTN: Jerry L. Harper

Lockheed Missiles and Space Co., Inc.
    ATTN: F. G. Borgardt
    ATTN: Raymond P. Capiaux
    ATTN: Lloyd F. Chase
    ATTN: S. P. Hardt

Martin Marietta Aerospace
Orlando Division
    ATTN: Laird Kinnaird

McDonnell Douglas Corporation
    ATTN: J. F. Garibotti
    ATTN: L. Cohen
    ATTN: R. J. Reck
    ATTN: J. Kirby

National Academy of Sciences
    ATTN: National Materials Advisory Board for
          Donald G. Groves

Northrop Corporation
    ATTN: Don Hicks

DEPARTMENT OF DEFENSE CONTRACTORS (Continued)

Physics International Company
    ATTN: Doc. Control for James Shea

Prototype Development Associates, Inc.
    ATTN: John Slaughter

R & D Associates
    ATTN: Albert L. Latter
    ATTN: Jerry Carpenter
    ATTN: F. A. Field
    ATTN: Harold L. Brode

Sciences Applications, Inc.
    ATTN: G. Ray
    ATTN: R. Fisher

Southern Research Institute
    ATTN: C. D. Pears

SRI International
    ATTN: Donald Curran
    ATTN: George R. Abrahamson
    ATTN: Herbert E. Lindberg
    ATTN: D. C. Erlich

Systems, Science and Software, Inc.
    ATTN: Russell E. Duff
    ATTN: G. A. Gurtman

Terra Tek, Inc.
    ATTN: Sidney Green

Aeronautical Rsch. Assoc. of Princeton, Inc.
    ATTN: Coleman Donaldson

SRI International
    ATTN: Harold Carey